

1 **Aseismic Fault Slip during a Shallow Normal-Faulting**
2 **Seismic Swarm Constrained Using a**
3 **Physically-Informed Geodetic Inversion Method**

4 **Yu Jiang¹, Sergey V. Samsonov², and Pablo J. González^{1,3}**

5 ¹COMET, Dept. Earth, Ocean and Ecological Sciences, School of Environmental Sciences, University of
6 Liverpool, Liverpool, L69 3BX, United Kingdom

7 ²Canada Centre for Mapping and Earth Observation, Natural Resources Canada, 560 Rochester Street,
8 Ottawa, ON K1S5K2, Canada

9 ³Department of Life and Earth Sciences, Instituto de Productos Naturales y Agrobiología (IPNA-CSIC),
10 38206 La Laguna, Tenerife, Canary Islands, Spain

11 **Key Points:**

- 12 • We estimate time-dependent fault slip to interpret geodetic data (wrapped phase
13 InSAR) by adapting an experimental laboratory-derived model.
- 14 • The 2011 Hawthorne shallow seismic swarm migrated from south to north, ini-
15 tiated as aseismic slip preceding the most energetic event M4.6.
- 16 • Slip evolution shares similar slip rates with other slow-slip phenomena, implying
17 that aseismic processes play a notable role during swarms.

Corresponding author: Yu Jiang, Yu.Jiang@liverpool.ac.uk

18 **Abstract**

19 Improved imaging of the spatio-temporal growth of fault slip is crucial for understand-
20 ing driving mechanisms of earthquakes and faulting. This is especially critical to prop-
21 erly evaluate the evolution of seismic swarms and earthquake precursory phenomena. Fault
22 slip inversion is an ill-posed problem and hence regularization is required to obtain sta-
23 ble and interpretable solutions. An analysis of compiled finite fault slip models shows
24 that slip distributions can be approximated with a generic elliptical shape, particularly
25 well for $M \leq 7.5$ events. Therefore, we introduce a new physically-informed regulariza-
26 tion to constrain the spatial pattern of fault slip distribution. Our approach adapts a
27 crack model derived from mechanical laboratory experiments and extends it to allow for
28 complex slipping patterns by stacking multiple cracks. The new inversion method suc-
29 cessfully recovered different simulated time-dependent patterns of slip propagation, i.e.,
30 crack-like and pulse-like ruptures, directly using wrapped InSAR phase observations. We
31 find that the new method reduces model parameter space, and favors simpler interpretable
32 spatio-temporal fault slip distributions. We apply the proposed method to the 2011 March-
33 September normal-faulting seismic swarm at Hawthorne (Nevada, USA), by computing
34 ENVISAT and RADARSAT-2 interferograms to estimate the spatio-temporal evolution
35 of fault slip distribution. The results show that (1) aseismic slip might play a significant
36 role during the initial stage, and (2) this shallow seismic swarm had slip rates consistent
37 with those of slow earthquake processes. The newly proposed method will be useful in
38 retrieving time-dependent fault slip evolution, and is expected to be widely applicable
39 to study fault mechanics, particularly in slow earthquakes.

Plain Language Summary

41 A key earthquake science challenge is to understand when an instability on a fault
42 will arrest or run away into a large rupture. However, the slip nucleation process seems
43 not to produce seismic waves and hence remains hidden to most seismological methods.
44 Geodetic methods, which can directly measure motions at earth's surface, offer a com-
45plementary tool to improve our ability to map the fault slip. In this work, we expand
46an experimentally observed crack model, and propose a new inversion method for find-
47ing models of fault slip that can fit the observations of surface motions. The new method
48greatly reduces computation complexity respecting previous state-of-the-art methods,
49and is validated against synthetic experiments. We apply this new method to 2011 Hawthorne
50earthquake swarm (Nevada, USA), and discovered an aseismic slow slip before seismic-
51ity rate increased. That preparation stage was followed by a triggered larger slip on a
52nearby fault, and after that, the seismicity and fault slip rate reduced rapidly. We ex-
53pect that this new methodology will be applied to detect similar precursory aseismic slip
54during long-lasting earthquake sequences, and allow us to retrieve detailed slip growth
55in space and time, which ultimately will advance our understanding of the faulting me-
56chanics.

1 Introduction

How fault slip nucleates, grows and eventually accelerates is a critical question to describe the driving mechanisms behind earthquakes and faulting phenomena. Our current understanding is consistent with various mechanisms to initiate fault slip: dynamic triggering (Gomberg & Johnson, 2005), tidal triggering (Delorey et al., 2017), pore-pressure diffusion (Parotidis et al., 2003) or aseismic slip (Radiguet et al., 2016; Gualandi et al., 2017; Caballero et al., 2021). In particular, Gomberg (2018) summarized two leading hypotheses for earthquake nucleation. One proposes a stochastic model in which each earthquake triggers subsequent ones in a cascade fashion, while the other favors a deterministic view where slow-slip triggers and precedes the occurrence of a seismically dynamic rupture. Within the scope of distinguishing between the two earthquake nucleation models, one opportunity is to increase our ability to image how fault slip evolves in space and time. Although fault slip evolution is not necessarily the only cause of seismicity migrating, it may provide crucial data to examine various hypotheses for earthquake nucleation mechanisms.

Fault slip propagation has characteristics that permit discriminating between regular earthquakes and slow-slip phenomena, such as slip rate. For regular earthquakes, the peak and average slip rate are of the order of 1 m/s and 0.1 m/s (Takenaka & Fujii, 2008). For slow-slip phenomena, slip rates are much lower, e.g., Slow Slip Events (SSEs), fault creep, or slip related to fluid injection. The range of peak slip rate in SSEs on subduction zones is 0.1~3 cm/day (Radiguet et al., 2011; Bletery & Nocquet, 2020; Rousset et al., 2019; Ozawa et al., 2019), whereas the fast slip rate in episodic creep events on the continental faults are 0.5~3 cm/year (Schmidt et al., 2005; Jolivet et al., 2012; Hussain et al., 2016; Scott et al., 2020). In fluid injection experiments, the slip rate has been observed to be much higher, up to 4×10^{-3} mm/s (35 cm/day) (Guglielmi et al., 2015).

To evaluate fault slip characteristics, a better description of how fault slip propagates in space and time is necessary. Two propagation patterns of seismic rupture were described in Lambert et al. (2021) and Marone and Richardson (2006): pulse-like and crack-like ruptures. The two distinguishable patterns are also observed in slow-slip phenomena: slow slip could either migrate further and further away from where it started along strike (or dip), or stay almost stationary through time. Observations of some SSEs

89 and "Episodic Tremor and Slip" (ETS) show that they are pulse-like ruptures with elon-
90 gated slipping areas on some subductions zones and follow the first pattern, e.g., the Cas-
91 cadia subduction zone (Michel et al., 2019). For the migration along strike, the migra-
92 tion speed is ~ 10 km/day (Wech et al., 2009; Rousset et al., 2019). In contrast, slip prop-
93 agation in the meter-scale fluid injection experiment follows the second pattern. Bhattacharya
94 and Viesca (2019) proposed a model in which the slip grows like expanding ellipses, with
95 the injection point as the slipping center. The latter phenomenon is also found in some
96 SSEs on subduction zones, e.g., the deeper Manawatu and Kaimanawa SSEs on the Hiku-
97 rangi subduction zone (Wallace, 2020).

98 In this research, we developed a new method to interpret directly wrapped phase
99 InSAR observations to estimate the spatio-temporal fault slip, in particular, in the con-
100 text of continental seismic swarms (e.g., small-amplitude surface deformation signals and/or
101 phase discontinuities due to surface ruptures). InSAR has been used to map surface dis-
102 placements with high spatial resolution and subsequently model fault slip. But so far,
103 it is more common to estimate static slip distributions than jointly invert for the time-
104 series of slip evolution (Floyd et al., 2016; Ingleby et al., 2020). The problem of retriev-
105 ing time series of source parameters from non-simultaneous and temporally overlapped
106 multi-sensor observations is ill-posed; however, the oscillations of the solution caused by
107 the rank deficiency of this problem can be reduced by applying regularization or tem-
108 poral filtering (Samsonov & D'Oreye, 2012). Grandin et al. (2010) introduced a tempo-
109 ral smoothing scheme as an additional constraint to retrieve the time series of magma
110 volume changes. Additionally, González et al. (2013) used truncated singular value de-
111 composition (TSVD) to reject model space basis vectors associated with small singular
112 values. Instead of regularizing the volume variation itself, they minimized the volume
113 change rate, to avoid large discontinuities. Here, we improve previous methods by a) reg-
114 ularizing the fault slip distribution using a prescribed parametrization derived from a
115 laboratory-based crack model, and b) introducing a statistically optimal truncation cri-
116 terion that allows to automatically separate signal and noise in the spatio-temporal fault
117 slip distributions. We demonstrated the validity of this approach using synthetic exper-
118 iments and comparing it against a compilation of published slip distribution models. Fi-
119 nally, we applied the new proposed methodology to the 2011 Hawthorne seismic swarm
120 (Nevada, USA). The 2011 Hawthorne seismic swarm is located at the central Walker Lane,
121 which accommodates the Pacific-North American transform plate motion by oblique-normal

122 faults and block rotations. The 2011 Hawthorne swarm consists of 10 M4+ events, and
123 the largest earthquake among them is a M4.6 event (Zha et al., 2019; Smith et al., 2011);
124 recent study using satellite images reveals clear surface deformation signals before the
125 M4.6 event, and the geodetic moment is much higher than the seismic moment, indicat-
126 ing that aseismic slip dominates the fault behavior (Jiang & González, 2021). By apply-
127 ing our newly proposed methodology, we retrieved the fault-slip spatio-temporal evolu-
128 tion, and the results will help us to better understand the fault mechanics and seismic
129 hazard in Walker Lane.

130 **2 Time-Dependent Fault Slip Inferred Using Geodetic Fault Slip Mod-** 131 **els**

132 **2.1 Static Fault Slip Models**

133 Slip inversions with kinematic models are ill-posed problems in which the solution
134 is nonunique and unstable, and unphysical slip distributions can be estimated by Least-
135 Square algorithms, i.e., extremely rough oscillatory slip distributions. Harris and Segall
136 (1987) introduced Laplacian smoothing as the regularization scheme. This minimizes the
137 second derivative of slip and can prevent cases with large stress drops. Du et al. (1992)
138 plotted a trade-off curve for misfit as a function of slip roughness, and manually picked
139 a smoothing factor within the inflection point of the curve to find an optimal balance
140 between data fit and model roughness. Matthews and Segall (1993) determined the op-
141 timal smoothing factor in the trade-off curve objectively by implementing the cross-validation
142 method. Much later, Fukahata and Wright (2008) and Fukuda and Johnson (2008) in-
143 troduced the Bayesian approach, ABIC (Akaike’s Bayesian Information Criterion), to
144 solve the slip distribution. While Fukahata and Wright (2008) emphasized the signifi-
145 cance of fault geometry as a nonlinear constraint, Fukuda and Johnson (2008) overcame
146 the deficiencies of ABIC with positivity constraints, and then applied the adapted ABIC
147 to simultaneously estimate the slip distribution and smoothing parameter objectively in
148 a Bayesian framework. Fukuda and Johnson (2010) then devised a mixed linear-non-linear
149 Bayesian inverse formulation and extended their work for the joint slip and geometry in-
150 version. In response, Minson et al. (2013) argued that the non-physical regularization
151 scheme (i.e., Laplacian smoothing) is unnecessary, and developed a fully Bayesian ap-
152 proach to sample all possible families of models compatible with the observations, via
153 a parallel computing framework. Ragon et al. (2018) further extended the work of Minson

154 et al. (2013) and accounted for the uncertainty in fault geometry. Instead of Laplacian
 155 regularization, Amey et al. (2018) developed an inversion package *slipBERI*, and incor-
 156 porated self-similarity, characterizing the seismic slip distribution in real earthquakes,
 157 as a prior assumption within the Bayesian inversion of earthquake slip.

158 All the previous methods are based on kinematic models that do not take into ac-
 159 count the relationship between stress and slip in the fault. Alternatively, dynamic source
 160 models satisfy physical constraints on the propagation of shear fractures on Earth, but
 161 few dynamic source models are considered to constrain the slip inversions. As an alter-
 162 native, Di Carli et al. (2010) proposed using elliptical patches to describe the slip dis-
 163 tribution in the kinematic and dynamic inversion of near-field strong motion data at low
 164 frequencies. Soon afterward, Sun et al. (2011) put forward a *mechanical* slip inversion,
 165 imposing a uniform stress drop on the fault plane. The resulting slip distribution is in-
 166 herently smooth, so the smoothing norm and the smoothing factor are unnecessary. Tridon
 167 et al. (2016) assumed a circular stress patch in volcano research, inverting the displace-
 168 ment for shear and normal stresses simultaneously, along with the fault geometry.

169 In this study, we present a Geodetic fault-slip Inversion using a physics-based Crack
 170 Model (GICMo), developed and demonstrated by Jiang et al. (2021). A one-dimensional
 171 analytical crack model is proposed by Ke et al. (2020), and it fits experimental labora-
 172 tory earthquake measurements of ruptures contained within a 3-meter-long saw-cut gran-
 173 ite fault. This new crack model features non-singular (finite) peak stresses at the rup-
 174 ture tip. Jiang et al. (2021) expanded the one-dimensional model into two-dimensional
 175 within an elliptical shape, by assuming one of the focal points of the ellipse to be the crack
 176 center (with the maximum slip) and the elliptical perimeter to be the crack tip. There-
 177 fore, the slip distribution on the fault plane is controlled by a very compact and reduced
 178 set of parameters. The geodetic-inverted fault slip infers that it is possible that the crack
 179 center can be located at the rupture center, e.g., 2009 L'Aquila earthquake (Walters et
 180 al., 2009). So we relax the constraint of the crack center location, and allow it to move
 181 along the x axis inside the ellipse. Our crack model contains only eight parameters as
 182 demonstrated by Equation 1 and Figure 1.

$$s = \mathbf{f}(x_0, y_0, a, e, \alpha, \lambda, d_{max}, \theta) \quad (1)$$

183 where s is the slip distribution; x_0, y_0 are the locations of the crack center; a and e are
 184 the semi-major axis and eccentricity of the ellipse; α is the ratio controlling the location

185 of crack center along x axis: the crack center is located at the ellipse center, left/right
 186 vertices when $\alpha = 0, -1/1$; λ is the ratio controlling the displacement transition from
 187 the center to the edge of the elliptical crack; d_{max} is the maximum slip; θ is the rake an-
 188 gle.

189 In the GICMo method, once the crack model parameters are provided, the slips
 190 for all fault patches are then determined based on the two-dimensional crack model dis-
 191 cussed above. Then, the fault slip distribution is forward modeled to estimate surface
 192 displacement. Following Jiang and González (2020), a misfit function is constructed based
 193 on the wrapped phase residuals and the weighting matrix. The misfit function is then
 194 regarded as the likelihood function fed into the Bayesian process to retrieve the poste-
 195 rior distribution of crack model parameters. In the Bayesian process, the Markov chain
 196 Monte Carlo algorithm is adopted as the probability sampling approach based on the
 197 Metropolis-Hasting rule.

198 Here we design a synthetic static slip to compare the performance of our method,
 199 GICMo, and a state-of-the-art method, slipBERI (Amey et al., 2018). The geodetic in-
 200 version package, slipBERI, solves for fault slip with GNSS and unwrapped InSAR phases
 201 in a Bayesian approach using von Karman regularization, and simultaneously solves for
 202 a hyperparameter that controls the degree of regularization. A normal fault with pure
 203 down-dip slip is simulated as the synthetic fault model. To imitate the slipping patterns
 204 observed in the published finite-source rupture models SRCMOD (Mai & Thingbaijam,
 205 2014) (e.g., Bennett et al. (1995), Ichinose et al. (2003), and Elliott et al. (2010)), the
 206 inner region is a square area with a larger displacement, and the outer region is an an-
 207 nulus area with a smaller displacement (Figure 2). Due to the difference in the inges-
 208 tion data, the synthetic phases are unwrapped phases for slipBERI and wrapped phases
 209 for GICMo. The displacement phase is forward calculated based on the synthetic fault
 210 slip distribution and the dislocation model. To increase its resemblance to reality, decor-
 211 relation and atmosphere noises are simulated and added, whose amplitudes are 10% of
 212 2π for wrapped phase cases or the peak amplitude of the deformation phase for unwrapped
 213 phase cases, which is based on the signal-to-noise ratio from a real interferogram in Sec-
 214 tion 4 (RS2-20110322-20110415). The simulated noise-plus-deformation interferogram
 215 is resampled with a quadtree algorithm within the downsampled unwrapped and wrapped
 216 phases (Bagnardi & Hooper, 2018; Jiang & González, 2020). In addition, the covariance
 217 matrix is estimated based on the phase in the far-field. Finally, the downsampled phases

218 and covariance matrix are fed into slipBERI and GICMo to retrieve the slip distribu-
 219 tions. Figures 2b-2d show the modeled slip distribution inverted by GICMo and slipBERI,
 220 and Figure S1 shows the modeled phase and phase residuals. The conclusions are listed
 221 below.

222 (1) Both GICMo and slipBERI provide the first-order accuracy of the slip distri-
 223 bution, including the locations of the crack center and the magnitude of the slip peak.

224 (2) We interpolate the slip distribution onto a $0.5 \text{ km} \times 0.5 \text{ km}$ patch mesh, and
 225 calculate the root-mean-square (RMS) of the slip distribution compared with the syn-
 226 thetic slip distribution. We find that the RMSs are 1.5 cm for one-ellipse model, 2 cm
 227 for von Karman smoothing model, and 3 cm for Laplacian smoothing model, which are
 228 approximately similar. However, the great advantage is that the parameters to be solved
 229 in GICMo are independent of the fault mesh discretization, and the number of param-
 230 eters is 30 times less in this case than 201 in slipBERI for this case.

231 **2.2 Bayesian Inversion of Fault Slip Time-Series Using a Physics-based** 232 **Crack Model (Time-GICMo)**

233 The temporal evolution of fault slip is critical to understanding the driving mech-
 234 anism of slow slip. It is difficult to find one slow slip event where one interferogram can
 235 coincidentally capture the beginning and the ending of the activity. Instead, a common
 236 scenario is that the slip increment is captured by interferograms. In this section, we de-
 237 velop a new method of retrieving the slip increments and demonstrate the time-series
 238 slip estimation with synthetic experiments. Assuming two elliptical ruptures at the be-
 239 ginning and the ending, slip increment $\Delta s = s^2 - s^1$, where s^2 and s^1 are the slip dis-
 240 tributions at the end and the beginning of the interferogram.

241 We consider a system of N increments of fault slip ($\Delta s^n \in [\Delta s^1, \dots, \Delta s^N]$) between
 242 dates t_i^n and t_j^n) based on the non-linear inversion estimation from the corresponding wrapped
 243 interferogram, and the raw images of interferograms are acquired at M unique dates ($t \in$
 244 $[t_1, \dots, t_M]$). The aim is to solve for the temporal evolution of fault slips ($s \in [s_1, \dots, s_M]$)
 245 for each date. We assume that the slip rate between adjacent dates ($v_m \in [v_1, \dots, v_{M-1}]$)
 246 are constant, so the slip increment Δs^n can be expressed by the sum of fault slip incre-
 247 ment between adjacent dates, $\Delta s^n = \sum_{m=i}^{j-1} v_m (t_{m+1}^n - t_m^n)$. The linear expression for
 248 N increments of fault slip is shown in Equation 2, as illustrated by González et al. (2013):

$$\begin{aligned}
\mathbf{P} &= \mathbf{B}\mathbf{Q} \\
\mathbf{P} &= [\Delta s^1 \quad \cdots \quad \Delta s^n \quad \cdots \quad \Delta s^N]^T \\
\mathbf{Q} &= [v_1 \quad \cdots \quad v_m \quad \cdots \quad v_{M-1}]^T \\
\mathbf{B}(n, m) &= \begin{cases} t_{m+1}^n - t_m^n, & \text{if } i \leq m \leq j - 1. \\ 0, & \text{otherwise.} \end{cases} \quad (2)
\end{aligned}$$

249 where \mathbf{P} is the observation vector, \mathbf{Q} the unknown vector, and \mathbf{B} the designed matrix.
250 Considering there are N increments of fault slip, the matrix dimension is $(N \times 1)$ for
251 \mathbf{P} , $(N \times (M - 1))$ for \mathbf{B} , and $((M - 1) \times 1)$ for \mathbf{Q} . Then, we decompose matrix \mathbf{B} by
252 using the SVD methods,

$$\mathbf{B} = \mathbf{U}\mathbf{S}\mathbf{V}^T \quad (3)$$

253 where \mathbf{U} is an orthogonal matrix with columns that are the basis vectors of the data space
254 $(N \times N)$, \mathbf{V} is an orthogonal matrix with columns that are the basis vectors spanning
255 the singular values of the model $((M - 1) \times (M - 1))$, and \mathbf{S} is a diagonal matrix of
256 the singular values $((N \times (M - 1)) \times 1)$. A solution for this problem can be obtained
257 as follows,

$$\mathbf{Q} = \mathbf{V}\mathbf{S}^{-1}\mathbf{U}^T\mathbf{P} \quad (4)$$

258 If $\text{rank}(\mathbf{B}) < m$, the solution obtained using the SVD technique may contain numerical
259 instabilities when there are small singular values. In this case, a more stable solution can
260 be achieved using the TSVD method (Aster et al., 2019), which rejects model space ba-
261 sis vectors associated with small singular values, up to a certain threshold. As an im-
262 provement on González et al. (2013), we apply an optimal hard threshold for singular
263 values proposed by Gavish and Donoho (2014). Gavish and Donoho (2014) proposed that
264 the optimal hard threshold for singular value is $4/\sqrt{3}$ of the median singular value. This
265 criterion is empirically proven to be the best hard thresholding, independent of model
266 size, noise level, or true rank of the low-rank model. This improvement allows us to de-
267 fine the degree of regularization based on objective criteria, which generates a low-rank
268 model from noisy data. Note that in order to retrieve a realistic solution, a non-negative
269 constraint is added in solving for slip rate vector Q implemented by using MATLAB func-
270 tion *lsqnonneg* (<https://uk.mathworks.com/help/optim/ug/lsqnonneg.html>). It is

271 physically appropriate because a fault is rarely observed to move backward, with only
 272 one known example (Hicks et al., 2020).

273 **3 Time-dependent Fault Slip Inversion Experiments**

274 In this section, we describe two experiments to simulate pulse-like and crack-like
 275 rupture propagation patterns in space and time. We tested the performance of the in-
 276 version method to recover fault slip evolution from each of the two-ellipse model.

277 The first synthetic case aims to explore the inversion with overlapping ruptures (Fig-
 278 ure 3). A number of recent studies have suggested spatial overlap between coseismic slip
 279 and afterslip (Barnhart et al., 2016; Bedford et al., 2013; Bürgmann et al., 2002; John-
 280 son et al., 2012; Pritchard & Simons, 2006; Salman et al., 2017; Tsang et al., 2016). A
 281 series of overlapping elliptical cracks are simulated in Figure 3a, and a forward inversion
 282 is performed to calculate the surface displacement due to the slip increment between ad-
 283 jacent cracks. We aimed to compare the results based on various geodetic inversion al-
 284 gorithms: (1) the one-ellipse model, as described in Section 2.1, (2) a von Karman reg-
 285 ularization algorithm (Amey et al., 2018), (3) the two-ellipse model with different crack
 286 centers. Inversions results are shown in Figures 3b-3d, and the modeled phase and resid-
 287 uals are shown in Figures S2-S3. The main conclusions are as follows.

288 (1) The RMS of the fault slip residual is the lowest in results based on the two-ellipse
 289 model with different centers. The triangle patch size in the crack model is ~ 0.84 km, and
 290 the rectangle patch size in slipBERI is 1.5 km. In this way, we interpolated the modeled
 291 slip distributions to grid points with 1.17 km spacing, and then calculated the RMS of
 292 the fault slip residual. In each case, the RMS of slip residuals based on the two-ellipse
 293 model with different centers (Figure 3d) are the smallest, and the average RMS for one-
 294 ellipse model, von Karman smoothing model and the two-ellipse model are 0.9 cm, 1.6
 295 cm, and 0.6 cm.

296 (2) The two-ellipse model is superior to the one-ellipse model in the F-test for the
 297 residual of the interferometric phase. The two-ellipse model has more free parameters,
 298 leading to an inherent improvement in the data fit. To objectively compare the model
 299 performances, we use F-ratio statistic to test the significance of decrease of residuals be-
 300 tween models (Stein & Gordon, 1984). The statistical test checks if the empirical F-ratio
 301 (F_{emp}) is larger than the theoretical (F_{theory}). In this case, the comparison of the one-
 302 ellipse model and two-ellipse model leads to $F_{emp} = 72.8 \gg F_{theory} = 2.6$.

303 The second synthetic case aims to explore the inversion with the containing rup-
 304 tures (Figure 4). A growing rupture has been widely observed and studied in fluid in-
 305 jection experiments (Guglielmi et al., 2015; Bhattacharya & Viesca, 2019; Cappa et al.,
 306 2019). The rupture center is located at the injection point, and the radius of the slip-
 307 ping zone grows at a rate up to 10^{-6} m/s. A set containing elliptical ruptures is sim-
 308 ulated in Figure 4a, and a forward inversion facilitates the surface displacement calcu-
 309 lation. We aimed to retrieve the slip increments from the observed interferometric phase
 310 with various methods described above (one-ellipse model, von Karman smoothing model,
 311 and two-ellipse model). On noticing that the slip distribution is not well resolved by the
 312 two-ellipse model with different centers, we added another constraint to the two-ellipse
 313 model so that both cracks share the same center. The inversion results are shown in Fig-
 314 ures 4b-4e, and the modeled phase and residuals are shown in Figures S4-S5. The main
 315 conclusions are as follows.

316 (1) The average RMS of slip residuals based on various inversion models (one-ellipse
 317 model, von Karman smoothing model, two-ellipse model with different centers, and one
 318 center) are 1.3 cm, 1.3 cm, 1.0 cm, and 0.8 cm. The one-ellipse model failed because the
 319 slip increment in containing ruptures no longer could be described by one complete crack.
 320 Indeed, slipBERI showed better performance because it inferred the region with the slip
 321 peak. The two-ellipse model with different centers is even better but was not well resolved,
 322 e.g., the slip increment from t_1 to t_2 (second image in Figure 4c). Therefore, the two-
 323 ellipse model with the *same* center is the most appropriate in reconstructing the cracks'
 324 locations, sizes, and maximum slips.

325 (2) In the F-test of the interferometric phase residuals, the two-ellipse model with
 326 the same center is superior to the two-ellipse model with different centers, and the one-
 327 ellipse model is the least useful model.

328 **4 Application case: the 2011 Hawthorne Seismic Swarm (Nevada, USA)**

329 **4.1 Regional Tectonics and Seismicity**

330 In this study, we focus on the 2011 Hawthorne seismic swarm, which occurred on
 331 the central Walker Lane (Figure 5). The Walker Lane is a 500 km-long and 100 km-wide
 332 deformation region consisting of N-NW right-lateral shear and extension (Wesnousky,
 333 2005). It is located between the northwest translating Sierra Nevada microplate and the
 334 westward extending Basin and Range Province. The Walker Lane accommodates 20%

335 $\sim 25\%$ of the current relative motion (50mm/year) between the Pacific and North Amer-
336 ican plates (Argus & Gordon, 1991; Faulds & Henry, 2008). The central Walker Lane
337 accommodates the deformation budget of ~ 8 mm/year between the Basin and Range
338 province and the central Sierra Nevada (Bormann et al., 2016). The distributed dextral
339 shear in central Walker Lane is accommodated by oblique-normal faults, block rotations,
340 and partitioning of oblique deformation between sub-parallel normal and strike-slip faults.
341 The total long-term strain rate is 51 nanostrain/year extension directed $N77^\circ W$ and 38
342 nanostrain/year contraction directed $N13^\circ E$ (Kreemer et al., 2014), much higher than
343 the central Basin and Range (Kreemer et al., 2009).

344 Being a geologically young and developing fault system, the Walker Lane under-
345 went long-lasting seismicity over the instrument period, including >10 M6+ earthquakes
346 in the last century, and it is regarded as a natural laboratory to study seismicity and fault
347 mechanics and to evaluate the seismic hazard in Southern California (Wesnousky, 2021).
348 A few seismic sequences struck the Walker Lane since 2000, e.g., the 2008 Mogul earth-
349 quake sequence (Ruhl et al., 2016, 2017), the 2011 and 2016 Hawthorne seismic swarm
350 (Smith et al., 2011), the 2017 Truckee sequence (Hatch et al., 2018), the 2014 Virginia
351 City Swarm (Hatch et al., 2020), the 2016 Nine Mile Ranch sequence (Hatch, 2020), the
352 2020 Monte Cristo Range sequence (Ruhl et al., 2021). The 2011 Hawthorne seismic swarm
353 lasted from March to September and consisted of 10 M4+ earthquakes according to the
354 U.S. Geological Survey (USGS) hypocentre catalog ([https://earthquake.usgs.gov/
355 earthquakes/search/](https://earthquake.usgs.gov/earthquakes/search/)). This sequence occurred in the footwall block of the Wassuk Range
356 segment at the central Walker Lane (Faulds & Henry, 2008), and this segment experi-
357 ences a significant extension of 1.5 ± 0.3 mm/year (Hammond & Thatcher, 2007). Early
358 moment tensor solutions show the shallow depths in this sequence (Smith et al., 2011),
359 and further hypocenter relocation together with the focal mechanisms of the M4+ events
360 consistently reveal a W-NW-dipping normal fault zone with centroid depths between 2
361 km and 4 km (Zha et al., 2019). The 2011 Hawthorne sequence is close to the Aurora-
362 Bodie volcano (Lange & Carmichael, 1996), but no volcanic signature was observed in
363 near-source seismograms, which infers this sequence is not likely related to the magmatic
364 activity (Smith et al., 2011; Zha et al., 2019). In this research, we identify three stages
365 with respect to the time when the most energetic event (M4.6) occurred: an initial stage
366 (pre-M4.6 stage) from 15 March to 17 April, the most energetic stage (co-M4.6 stage),
367 and the post-energetic stage (post-M4.6 stage) until 17 September.

4.2 Multi-satellite Geodetic Datasets

We processed ENVISAT and RADARSAT-2 data and generated 8 SAR interferograms to quantify surface displacements (Figure 6). SAR images were acquired between February and September 2011 from two tracks: one ascending track from the Canadian Space Agency RADARSAT-2 satellite, look angle 35° and heading angle 350° ; and another descending track from the European Space Agency (ESA) ENVISAT satellite, track 343, look angle 35° and heading angle -166° . Interferograms were processed in two-pass differential mode, using a 30m resolution digital elevation model (DEM) derived from the Shuttle Radar Topography Mission. ENVISAT-ASAR data were processed using Doris software (Kampes et al., 2003) and ISCE software, RADARSAT-2 data using GAMMA software (Werner, 2000). Overall, we obtained 8 short baseline differential interferograms. The computed interferograms have temporal separations ranging from 24 to 120 days. Considering the dominant extensional mechanism and N-S fault striking in this region, the preferred movement direction of the ground displacement is E-W. Consequently, the satellite flight direction favors surface displacement observations in this normal faulting system.

Interestingly, 2 ascending RADARSAT-2 interferograms during the pre-M4.6 stage indicated clear surface displacement signals (Figures 6d and 6a), ~ 4 cm away from satellite line-of-sight motion. In interferograms covering the co-M4.6 stage, it is notable that surface displacement signals were larger in magnitude and located further north with respect to the pre-M4.6 stage (Figures 6b, 6c, 6e and 6f). During the early post-M4.6 stage, surface displacements were detected along a very narrow spatial band with clear phase discontinuities, suggesting surface ruptures (Figure 6g). For one interferogram covering the late post-M4.6 stage (Figure 6h), the phase was dominated by atmospheric noise and no clear deformation signal was detected. Analysis of interferograms suggests that fault slip may have occurred along a fault system with a two-plane geometry, which is consistent with the finding from early moment tensor solutions (Smith et al., 2011).

4.3 Spatio-temporal Slip Evolution

To develop the kinematic fault model, we first constructed the fault geometry by applying a state-of-the-art inversion method, solving for uniform distribution on rectangular faults (Jiang & González, 2020). The geodetic inversion is directly using the in-

399 interferometric wrapped phase to avoid any potential phase unwrapping error (Figure S6).
 400 The data variance-covariances describing the noise level are calculated based on the co-
 401 variograms (Figure S7) and are used to weight the wrapped phase residuals in the like-
 402 lihood function as illustrated by Jiang and González (2020). Modeling of a selection of
 403 interferograms covering the successive phases confirmed that ground motion could be caused
 404 by fault geometry with two distinct planes. During the pre-M4.6 stage, the observed ground
 405 motion in the RADARSAT-2 interferogram (2011/03/22-2011/04/15, Figure 6d, and fault-
 406 normal profile in Figure 7d) would be consistent with slip along a N-S striking normal
 407 fault to the south (green rectangular fault in Figure 7a). After modeling the interfero-
 408 gram covering the co- and post-M4.6 stages (2011/04/15-2011/06/26, Figure 6f, and fault-
 409 normal profile in Figure 7c), Figure 6f shows a different fault segment on a NE-SW trend-
 410 ing normal fault to the north (yellow rectangular fault in Figure 7a). Based on modeled
 411 fault geometry in Figure 7a, together with ground motion discontinuities digitized from
 412 the interferograms, we constructed a smooth fault plane with uniformly discretized tri-
 413 angular meshes in Figure 7d. These were generated by FaultResampler (Barnhart & Lohman,
 414 2010) and mesh2d (Engwirda, 2014), with a near-uniform side length around 125 m. Then,
 415 a fault slip distribution model with associated uncertainties was estimated. We applied
 416 our newly developed fault slip inversion method, GICMo, based on a prescribed regu-
 417 larization derived from an experimentally validated physics-based crack model (Jiang
 418 et al., 2021). To further investigate the temporal evolution of fault slips with a higher
 419 temporal resolution, we invert the fault slip time-series using all available interferograms
 420 with clear deformation signals.

421 Figure 8 presents the temporal evolution of cumulative slip and slip rate during the
 422 2011 Hawthorne seismic swarm, and Figure S9 shows the modeled phase and phase resid-
 423 uals. The findings from the inversion results are listed as follows.

424 (1) There were three areas with different spatio-temporal slipping behaviors: a nar-
 425 row (5 km^2) slip area on the southern fault with a high rate (lower boundary: 1.5 cm/day,
 426 or $1.7 \times 10^{-7} \text{ m/s}$) occurring during the pre-M4.6 stage, a wider (15 km^2) slip area with
 427 lower average slip (10 cm) on the northern fault that ruptured during the co-M4.6 stage,
 428 and a shallow slip area (depth=1 km) just above the second area during the post-M4.6
 429 stage with a slower average slip rate (lower boundary: 0.2 cm/day, or $2.3 \times 10^{-8} \text{ m/s}$).

430 (2) Our results show the aseismic slip mainly occurred on the southern subfault dur-
 431 ing the pre-M4.6 stage, while the most significant seismic slip hit the northern subfault

432 during the co- and post-M4.6 stages. The results are more consistent with a cascade model
 433 of discrete slip patches, rather than a slow-slip model considered as a growing elliptical
 434 crack.

435 (3) During the early pre-M4.6 stage (February 26-March 22), the cumulative geode-
 436 tic moment is 1.7×10^{16} Nm (equivalent to a M_w 4.7 event), 45 times as large as the cu-
 437 mulative seismic moment (0.04×10^{16} Nm). The cumulative geodetic/seismic moment ra-
 438 tio reduces over time, but remains larger than 3 during the co- and post-M4.6 stages.

439 5 Discussion

440 5.1 On the Spatial Complexity of Fault Slip Distributions

441 Fault slip most likely has nonuniform spatial distribution due to spatial heterogeneities
 442 of rock strength and stress state on the fault, with well-known dependence on depth and
 443 the less understood along-strike variations. Seismic and geodetic inversions can reveal
 444 how fault slip is distributed on the discretized fault plane. However, to explore all pos-
 445 sible models consistent with observations, the parameter space scales up rapidly to a large
 446 number of unknowns, increasing the problem's null-space, which means there are many
 447 vectors in the model space that are unconstrained by the data. Therefore, it is reason-
 448 able to consider our understanding of the complexity of slip distribution in natural earth-
 449 quakes. The reasonable approach is able to allow for fault-slip heterogeneity, while keep-
 450 ing the problem null-space as small as possible. Mai and Beroza (2002) compiled pub-
 451 lished finite-source rupture models, and proposed the fractal pattern in slip distributions.
 452 It is true for large earthquakes, and multiple fault segments with several rupturing cen-
 453 ters are revealed by geodetic and seismological observations, e.g., 2008 M_w 7.9 Wenchuan
 454 earthquake (Shen et al., 2009), and 2016 M_w 7.8 Kaikoura earthquake (Hamling et al.,
 455 2017). However, solving a huge number of parameters has a high computation cost. Com-
 456 putation complexities in their algorithms depend greatly on the number of discretized
 457 fault patches. For example, when studying a 40 km-long and 20 km-wide fault with slip-
 458 BERT, there are 200 patches if the patch size is 2 km and the parameter' dimensions are
 459 400. The latter would rapidly increase to 1600 if the patch size is 1 km. This is possi-
 460 bly the reason why the number of imported fault patches has upper bounds in practice,
 461 particularly if a Bayesian sampling strategy is employed. Though techniques like par-
 462 allel computing have been introduced to improve computation efficiency, sampling such

463 high-dimensional problems is still computationally challenging and does not solve the
464 size of the null-space.

465 In this research effort, we favored a method that dramatically reduces the num-
466 ber of free parameters to solve; the drawback is that it results in *compact* fault slip dis-
467 tributions. However, our inverted slip distribution patterns are supported by the obser-
468 vations. This is a reasonable approach, because many inversion results support fault-slip
469 distributions that are spatially compact, especially for small-magnitude earthquakes (Taymaz
470 et al., 2007; Barnhart et al., 2014; Xu et al., 2016; Champenois et al., 2017; Ainscoe et
471 al., 2017). Many studies have successfully modeled the majority of surface displacement
472 signals using only one single fault with uniform distribution (Biggs et al., 2006; Nissen
473 et al., 2007; Walters et al., 2009). For slow slip events across the global subduction zones,
474 distribution patterns usually follow an elliptical shape with one slipping center (Wallace
475 et al., 2012; Villegas-Lanza et al., 2016; Fukuda, 2018), and the fractal pattern is not re-
476 quired.

477 Benefiting from the online database of finite fault rupture models, SRCMOD (Mai
478 & Thingbaijam, 2014), we were able to quantitatively evaluate how well a single ellip-
479 tical model fits the available slip distributions across various tectonic settings and mag-
480 nitudes. We retrieved 300 slip distributions on a single fault from SRCMOD, and intended
481 to model the slip distributions with the one-ellipse model. Our experiments showed that
482 for 85% of $M_w \leq 7.5$ events, the RMS of the slip residual is less than 20% of the peak
483 slip (Figure S10). In addition, a simple circular crack is also the widely accepted assumed
484 model in stress drop estimation based on seismic spectra (Madariaga, 1976; Kaneko &
485 Shearer, 2014). Though only small degrees of freedom is allowed in the one-ellipse model,
486 complexity could be added by incorporating multiple ruptures. As we showed in Section
487 2.2, a half-moon pattern was retrieved by two containing or overlapping elliptical crack
488 models. Similarly, it is possible to overlap multiple ruptures to simulate multiple peak
489 slips or more complex patterns.

490 The compact slip distribution in this new elliptical model is also favorable to eval-
491 uate the statistics of small earthquakes. Earthquake source parameters characterization
492 of small earthquakes is important for understanding the physics of source processes and
493 might be useful for earthquake forecasting (Uchide et al., 2014). A wide-used source model
494 to analyze the source parameters of small earthquakes is a circular crack rupture (Brune,
495 1970; Madariaga, 1976) with stress singularity at the crack tip, and we hope our new el-

496 liptical slip model, which avoids this stress singularly, can be an alternative source model
 497 in the future (Shearer et al., 2006). Furthermore, by taking advantage of the improved
 498 method for estimating slip rates during temporally overlapping InSAR timeframes, one
 499 can image the fault behavior over a long period in a relatively high temporal resolution.
 500 This new method is expected to be applied to investigate the temporal evolution of slow
 501 fault slip, e.g., transient slow slip (Khoshmanesh et al., 2015; Kyriakopoulos et al., 2013;
 502 Klein et al., 2018), afterslip (Thomas et al., 2014), and slow slip events in subduction
 503 zones (Bletery & Nocquet, 2020; Rousset et al., 2019; Ozawa et al., 2019).

504 **5.2 Time-dependent Fault Kinematics during Continental Seismic Swarms** 505 **and Other Slow Earthquakes**

506 During the initial stage of the 2011 Hawthorne seismic swarm, a substantial amount
 507 of aseismic slip ruptured on the southern subfault without strong seismicity (e.g., the
 508 first two periods in Figure 8b), with peak slip rates of 1.1~5.4 cm/day, average slip rate
 509 0.4~1.9 cm/day and migration velocity 0.05 km/day. The phenomena potentially driven
 510 by aseismic slip are widely explored, e.g., ETS, Rapid Tremor Reversals (RTRs), SSEs,
 511 fault creep, and fluid injection. To better compare this precursory aseismic slip with other
 512 identified phenomena in the slow slip family, we compile the slip rates and migration ve-
 513 locities found in the literature list below and in Table S1.

514 (1) The peak slip rate. SSEs show a wide range of peak slip rate among subduc-
 515 tion zones, e.g., 0.27 cm/day for Cascadia subduction zone (Bletery & Nocquet, 2020),
 516 0.3 cm/day for South Central Alaska Megathrust (Rousset et al., 2019), 0.6~2.8 cm/day
 517 for Japan trench (Hirose & Obara, 2010; Ozawa et al., 2019). During the early stage of
 518 the 2011 Peloponnese seismic swarm (Greece) (Kyriakopoulos et al., 2013), the fault be-
 519 havior was dominated by aseismic slip inferred from the geodetic and seismic moment,
 520 and the peak slip rate was 0.26 cm/day. The maximum slip rate in fault creep events
 521 are very low, e.g., 0.5 cm/year on the Hayward fault (Schmidt et al., 2005), 0.5 cm/year
 522 on the Haiyuan Fault (Jolivet et al., 2012; Song et al., 2019), 0.8 cm/year on the North
 523 Anatolia Fault (Hussain et al., 2016) and 3 cm/year on the San Andreas Fault (Johanson
 524 & Bürgmann, 2005; Khoshmanesh et al., 2015; Scott et al., 2020). However, in the fluid
 525 injection experiment the slow aseismic slip during the early stage was much higher, $4 \times$
 526 10^{-3} mm/s (35 cm/day) (Guglielmi et al., 2015), potentially because the measurement

527 in the fluid injection is real-time, and the duration uncertainty is much lower than SSEs
528 observations.

529 (2) The average rate of slip increment. Research on the 2010-2014 seismic swarm
530 in southern Italy (Cheloni et al., 2017) is consistent with our findings. This research re-
531 vealed that the average slip rate started to increase two months before the largest shock
532 (M_w 5.1) and reached the highest value, ~ 0.1 cm/day, a few days before the largest shock.
533 It then decreased to zero in the following months. This highest average slip rate was at
534 the same level with ~ 0.4 - 1.9 cm/day in our research. The aseismic slip rate inferred by
535 RE is much lower, ~ 0.3 - 3 cm/year (Nadeau & McEvilly, 1999; Turner et al., 2013; Mes-
536 imeri & Karakostas, 2018).

537 (3) Migration velocity. These velocities of ETS and SSEs vary with subduction zones
538 (Yamashita et al., 2015), but the generally reported migration velocity along the strike
539 of the plate geometry is ~ 10 km/day (Wech et al., 2009; Wallace et al., 2012), while RTRs
540 propagate ‘backward’ 20 to 40 times faster than ETS advances forward (Houston et al.,
541 2011). The large-scale features of ETS propagation with RTRs are reproduced and sup-
542 ported by numerical experiments (Luo & Liu, 2019; Liu et al., 2020). Similarly, migra-
543 tion velocity in TES varies over a wide range, from 0.5 to 14 km/day (Passarelli et al.,
544 2018; De Barros et al., 2020).

545 **5.3 Spatially variable mechanical response of the Hawthorne swarm faults**

546 As shown in Figure 8b, the southern segment is active during the pre-M4.6 stage,
547 and the fault behavior is mostly dominated by aseismic slip, inferred from a very high
548 geodetic/seismic moment ratio $\in [25, +\infty]$ (Figure 8c), while the general cumulative geode-
549 tic/seismic moment ratio remains larger than three for the whole seismic swarm. This
550 significant portion of aseismic slip identified here has been reported associated with a
551 handful of continental seismic swarms (Lohman & McGuire, 2007; Wicks et al., 2011;
552 Kyriakopoulos et al., 2013; Gualandi et al., 2017; Cheloni et al., 2017). In 2005, a tec-
553 tonic swarm of over a thousand earthquakes occurred in the Salton Trough, California
554 (USA) and Lohman and McGuire (2007) revealed the geodetic moment of the modeled
555 fault system was about seven times the cumulative seismic moment of the swarm. Wicks
556 et al. (2011) studied a swarm in southeastern Washington (USA) and also found the geode-
557 tic/seismic moment ratio was about seven. During the 2011 Peloponnese Peninsula seis-

558 mic swarm (Greece), Kyriakopoulos et al. (2013) revealed a big discrepancy of moment
559 release, where the geodetic moment was ~ 5 times the cumulative seismic moment for
560 the interval July 3-October 1. For the 2013-2014 Northern Apennines seismic swarm (Italy),
561 the moment associated with aseismic deformation/the seismic moment ratio is between
562 $70\% \pm 29\%$ and $200\% \pm 70\%$ (Gualandi et al., 2017). For the 2010-2014 Pollino seis-
563 mic swarm (Italy), Cheloni et al. (2017) found 70% of the moment was released aseis-
564 mically. Above all, though it is possible that the estimated geodetic moment could be
565 biased by the noise in the data or the inversion method, it cannot rule out that the sig-
566 nificant portion of seismic swarms are accompanied by aseismic slip, in the light of the
567 estimated ratios between the geodetic moment and seismic moment reaching high val-
568 ues, such as ~ 5 -8. Furthermore, the compact fault slip identified during the pre-M4.6
569 stage is favored by our improved methodology as demonstrated in Section 2. The pre-
570 vious finding of fractal distribution of fault slip is based on M5.9+ earthquakes (Mai &
571 Beroza, 2002), while small-to-moderate-magnitude ruptures would have more compact
572 slip distribution with low complexity as observed in the rupture models SRCMOD (Mai
573 & Thingbaijam, 2014). Therefore, we hope that our improved method can be used to
574 improve the detection of similar small-to-moderate-magnitude aseismic transients in fu-
575 ture seismic swarms.

576 The finding of the aseismic slip during the pre-M4.6 stage arises the question of whether
577 the largest M4.6 event could be controlled by the precursory slow slip, or either the pres-
578 lip model or the cascading model is supported. (1) In the preslip model, the preseismic
579 slip weakens the surrounding fault, and the magnitude of an earthquake is controlled pri-
580 marily by its nucleation process, e.g., the amplitude and area of precursory slip. As ob-
581 served in the laboratory experiments of frictional sliding (Ohnaka & Kuwahara, 1990;
582 Latour et al., 2013), the nucleation consists of two distinct stages, and both phases are
583 aseismic: (I) an initial quasi-static stage, and (II) the subsequent faster-accelerating stage.
584 We also observe similar acceleration pattern during the pre-M4.6 stage, where the me-
585 dian slip rate increased from 2×10^{-8} m/s (February 26~March 15) to 6×10^{-8} m/s (March
586 15~March 20). There is another possibility that the aseismic slip during the early stage
587 is an independent slow slip event, which is not related to the earthquake nucleation and
588 the triggering of the M4.6 event is incidental. We calculate the cumulative Coulomb stress
589 changes on the hypocenter of five M4+ foreshocks and the M4.6 event based on the mod-
590 eled slip and the maximum value of the cumulative Coulomb stress change over the seis-

591 mic rupture regions are 5.3, 6.9, 2.8, 3.9, 0.4, and 4.1 MPa, which is enough to trigger
592 an earthquake (King et al., 1994). (2) In the cascade model, earthquakes occur by neighbor-
593 to-neighbor stress transfer between one foreshock and another without an aseismic slip
594 component, and the eventual mainshock is a random outcome of triggering by ordinary
595 small earthquakes in close enough proximity to the mainshock (Ellsworth & Bulut, 2018).
596 Similarly, we calculate the cumulative Coulomb stress change on five M4+ events and
597 the M4.6 event caused by the earlier earthquakes and the maximum value of the cumu-
598 lative Coulomb stress changes over the seismic rupture regions is 0.7, 1.1, 3.0, 0.1, 1.1,
599 and 1.5 MPa, which is also higher than 0.01 MPa. It inferred that the M4+ foreshocks
600 and the M4.6 event can also be triggered by the earlier earthquakes. However, this anal-
601 ysis can be affected by many factors, e.g., the precision of earthquake hypocenter, and
602 the stress drop calculation method. For example, an M_w 4.3 foreshock occurred two hours
603 before the 1992 M_w 6.1 Joshua Tree earthquake, and Dodge et al. (1996) estimated the
604 Coulomb stress change from the foreshocks at the mainshock hypocenter by assuming
605 a circular source model with a constant stress drop crack model and placing the main-
606 shock hypocenter inside foreshock rupture. They found the Coulomb stress change was
607 almost certainly negative (99.9%) and concluded that the static stress change from the
608 foreshocks was unlikely to initiate the mainshock. In contrast, Mori (1996) calculated
609 a finite slip model for the foreshock where the mainshock hypocenter was outside of the
610 foreshock rupture, and he estimated a quite high stress drop of the foreshock (32~87 MPa)
611 on the mainshock hypocenter. The opposite conclusions from two different studies im-
612 ply the resolution limits of foreshock-location-based triggering analysis. To conclude, though
613 limitations in analyzing the Coulomb stress change, the triggering of earthquakes dur-
614 ing the initial phase cannot be explained by solely the cascade model, since the large dis-
615 agreement between the geodetic moment and the seismic moment indicates that seismic
616 slip cannot solely explain the observed surface deformation successfully. As for the largest
617 M4.6 event, we interpret it could have been triggered by earthquake nucleation initialed
618 by aseismic, an independent slow slip event, nearby preceding seismicity, or all of them.

619 The aseismic slip mainly occurred on the southern subfault during the pre-M4.6
620 stage, while the most significant seismic slip hit the northern subfault during the co- and
621 post-M4.6 stages. Here we discuss the possible underlying mechanisms of contrasting be-
622 haviors on the two subfaults. One potential cause of the precursory aseismic slip on the
623 southern segment is various dilatancy properties along strike. Many authors have stud-

624 ied the shear-induced dilatancy, which could increase the effective normal stress and thus
625 favor fault stability (Segall & Rice, 1995; Segall et al., 2010; Ciardo & Lecampion, 2019).
626 For example, to explain abundant microseismicity and aseismic transients in barrier zones
627 on the Gofar transform fault, Liu et al. (2020) proposed a numerical model where strong
628 dilatancy strengthening effectively stabilizes along-strike seismic rupture propagation and
629 results in rupture barriers where aseismic transients arise. If this is also true for the 2011
630 Hawthorne seismic swarm, the shear-induced dilatancy would explain the aseismic tran-
631 sients on the southern fault and the seismic rupture on the northern subfault. What’s
632 more, the requirement of enhanced fluid-filled porosity for the dilatancy strengthening
633 might be filled for the 2011 Hawthorne sequence. The 2011 Hawthorne sequence is close
634 to the Aurora-Bodie volcano (Lange & Carmichael, 1996), and geothermal fluids have
635 been found in this area (Hinz et al., 2010), so it is possible that excess fluids can be per-
636 sistently supplied and lead to large fluid-filled porosity and high pore pressure. There-
637 fore, the dilatancy strengthening might be one of the underlying mechanics that govern
638 the partitioning between aseismic and seismic slip during the 2011 Hawthorne earthquake
639 swarm.

640 In addition, the fault geometrical complexity could favor the lateral variation of
641 slip and aseismic slip. Firstly, Romanet et al. (2018) proposed that two overlapping faults
642 can naturally result in a complex seismic cycle without introducing complex frictional
643 heterogeneities on the fault. They found, for two mildly rate-weakening faults with a small
644 distance between the faults, a complex behavior with a mixture of slow and rapid slip
645 can be observed. This finding is consistent with the mixture of slow and fast slip close
646 to the connecting region of two subfaults during the 2011 Hawthorne swarm (triangu-
647 lar subfault in Figure 8). Secondly, Cattania and Segall (2021) highlights the effect of
648 long-wavelength fault roughness on a range of fault behaviors, foreshocks, and precu-
649 ratory slow slip, during the preparation stage of an energetic event. Their numerical sim-
650 ulation suggested the preparation stage is characterized by feedback between creep and
651 foreshocks: episodic seismic ruptures break neighboring asperity groups and favor the
652 creep acceleration, which loads other asperities leading to further foreshocks consecu-
653 tively. The coexistence of foreshocks and precursory slow slip, as well as their migration
654 toward the hypocenter of the energetic event in Cattania and Segall (2021), also matched
655 our observation during the pre-4.6 stage (Figure 8). Therefore, we think fault geomet-

656 rical complexity might contribute to the precursory slow slip during the 2011 Hawthorne
657 earthquake swarm.

658 **6 Conclusion**

659 This study has developed a new methodology for retrieving time-dependent fault
660 distributions, by incorporating a physics-based crack model. We first introduce two prop-
661 agation patterns of fault ruptures and then propose a method to solve the complex slip
662 distribution with multiple physics-based crack models. Finally, the proposed method-
663 ology is demonstrated by simulated experiments and one real seismic swarm case. The
664 advantages of the proposed method are as follows.

665 (1) To describe a compact slip distribution, a laboratory-derived crack model is used
666 in our inversion method, significantly reducing the number of parameters to solve, in-
667 dependently of the level of fault discretization. Though the degree of freedom is less than
668 in the previous methods, some complexity in the slip pattern can be incorporated by adding
669 multiple partially or totally overlapping ruptures.

670 (2) The robustness of our method has been demonstrated by simulated cases with
671 various slip patterns and published slip distribution datasets, SRCMOD.

672 (3) Our proposed method is applied to derive a time-dependent fault slip distri-
673 bution model for the 2011 Hawthorne seismic swarm (Nevada, USA). The results show
674 that aseismic slip on a southern subfault dominates fault behavior during the pre-M4.6
675 stage; then during the most energetic stage, the largest event occurred on a northern sub-
676 fault. Our results are consistent with an overlapping fault slip migration during the pre-
677 M4.6 stage along the southern fault, followed by larger triggered coseismic ruptures of
678 fault patches along the northern fault. Our model favors the identification of small-scale
679 compact slip distribution, and allows us to estimate the peak and average value of fault
680 slip rates. These are consistent with reported values for slow slip events and other con-
681 tinental swarms.

682 The new inversion method presented is complementary to the existing methodol-
683 ogy for retrieving fault-slip distributions. We hope it becomes a useful toolbox to im-
684 prove the identification of similar precursory slow slip during other long-lasting earth-
685 quake sequences (swarms), and help understand the driving mechanisms of earthquakes.

Acknowledgments

686
687 This research was supported by the Natural Environmental Research Council (NERC)
688 through the Centre for the Observation and Modeling of Earthquakes, Volcanoes and
689 Tectonics (UK) (GA/13/M/031) and the LiCS large grant (NE/K011006/1). This re-
690 search was also supported by a Chinese Scholarship Council-University of Liverpool joint
691 scholarship awarded to YJ (201706450071). PJG acknowledged the support of the Span-
692 ish Ministerio de Ciencia e Innovación research project, grant agreement number PID2019-
693 104571RA-I00 (COMPACT) and the Beca Leonardo a Investigadores y Creadores Cul-
694 turales 2020 from the Fundación BBVA. RADARSAT-2 images were acquired under SOAR-
695 E project 28209 from the Canadian Space Agency, and ENVISAT images from ESA CAT1
696 project 6745. RADARSAT-2 and ENVISAT interferograms in the paper can be down-
697 loaded from <https://doi.org/10.5281/zenodo.5043161>. The finite-fault source model
698 SRCMOD is retrieved from <http://equake-rc.info/srcmod/>. The geodetic inversion
699 software slipBERI is retrieved from <https://github.com/ruthamey/slipBERI> and WG-
700 BIS package from <https://doi.org/10.5281/zenodo.3727158>. The CRUST 1.0 model
701 is retrieved from <https://igppweb.ucsd.edu/~gabi/crust1.html>. The manuscript was
702 edited by Guido Jones, currently funded by the Cabildo de Tenerife, under the TFinnova
703 Programme supported by MEDI and FDCAN funds. Thanks go to Mehdi Nikkhoo for
704 providing the triangular dislocation functions for displacement gradient tensor. The au-
705 thors are also grateful to Tim Wright, Dan Faulkner, and Louisa Brotherson for insight-
706 ful discussions of different aspects of this study, as well as to editor Rachel Abercrom-
707 bie, associate editor, Eric Lindsey, and another anonymous reviewer for their helpful and
708 constructive reviews, which greatly improved this manuscript.

709 **References**

- 710 Ainscoe, E. A., Elliott, J. R., Copley, A., Craig, T. J., Li, T., Parsons, B. E., &
 711 Walker, R. T. (2017). Blind Thrusting, Surface Folding, and the Devel-
 712 opment of Geological Structure in the Mw 6.3 2015 Pishan (China) Earth-
 713 quake. *Journal of Geophysical Research: Solid Earth*, *122*(11), 9359–9382. doi:
 714 10.1002/2017JB014268
- 715 Amey, R. M. J., Hooper, A., & Walters, R. J. (2018). A Bayesian Method for Incor-
 716 porating Self-Similarity Into Earthquake Slip Inversions. *Journal of Geophysi-
 717 cal Research: Solid Earth*, *123*(7), 6052–6071. doi: 10.1029/2017JB015316
- 718 Argus, D. F., & Gordon, R. G. (1991). Current Sierra Nevada-North America mo-
 719 tion from very long baseline interferometry: Implications for the kinematics of
 720 the western United States. *Geology*, *19*(11), 1085–1088.
- 721 Aster, R. C., Borchers, B., & Thurber, C. H. (2019). Chapter three - rank deficiency
 722 and ill-conditioning. In R. C. Aster, B. Borchers, & C. H. Thurber (Eds.), *Pa-
 723 rameter estimation and inverse problems* (Third Edition ed., p. 55-91). Else-
 724 vier. doi: 10.1016/B978-0-12-804651-7.00008-0
- 725 Bagnardi, M., & Hooper, A. (2018). Inversion of Surface Deformation Data for
 726 Rapid Estimates of Source Parameters and Uncertainties: A Bayesian Ap-
 727 proach. *Geochemistry, Geophysics, Geosystems*, *19*(7), 2194–2211. doi:
 728 10.1029/2018GC007585
- 729 Barnhart, W. D., Benz, H. M., Hayes, G. P., Rubinstein, J. L., & Bergman,
 730 E. (2014). Seismological and geodetic constraints on the 2011 Mw5.3
 731 Trinidad, Colorado earthquake and induced deformation in the Raton Basin.
 732 *Journal of Geophysical Research: Solid Earth*, *119*(10), 7923–7933. doi:
 733 10.1002/2014JB011227
- 734 Barnhart, W. D., & Lohman, R. B. (2010). Automated fault model discretization
 735 for inversions for coseismic slip distributions. *Journal of Geophysical Research:
 736 Solid Earth*, *115*(B10). doi: 10.1029/2010JB007545
- 737 Barnhart, W. D., Murray, J. R., Briggs, R. W., Gomez, F., Miles, C. P., Svarc, J.,
 738 ... Stressler, B. J. (2016). Coseismic slip and early afterslip of the 2015 Il-
 739 lapel, Chile, earthquake: Implications for frictional heterogeneity and coastal
 740 uplift. *Journal of Geophysical Research: Solid Earth*, *121*(8), 6172–6191. doi:
 741 10.1002/2016JB013124

- 742 Bedford, J., Moreno, M., Baez, J. C., Lange, D., Tilmann, F., Rosenau, M., ... Vi-
 743 gny, C. (2013). A high-resolution, time-variable afterslip model for the 2010
 744 Maule Mw=8.8, Chile megathrust earthquake. *Earth and Planetary Science*
 745 *Letters*, *383*, 26–36. doi: 10.1016/j.epsl.2013.09.020
- 746 Bennett, R. A., Reilinger, R. E., Rodi, W., Yingping Li, Toksoz, M. N., & Hudnut,
 747 K. (1995). Coseismic fault slip associated with the 1992 M w 6.1 Joshua Tree,
 748 California, earthquake: Implications for the Joshua Tree-Landers earthquake
 749 sequence. *Journal of Geophysical Research: Solid Earth*, *100*(B4), 6443–6461.
 750 doi: 10.1029/94JB02944
- 751 Bhattacharya, P., & Viesca, R. C. (2019). Fluid-induced aseismic fault slip out-
 752 paces pore-fluid migration. *Science*, *364*(6439), 464–468. doi: 10.1126/science
 753 .aaw7354
- 754 Biggs, J., Bergman, E., Emmerson, B., Funning, G. J., Jackson, J., Parsons, B.,
 755 & Wright, T. J. (2006). Fault identification for buried strike-slip earth-
 756 quakes using InSAR: The 1994 and 2004 Al Hoceima, Morocco earth-
 757 quakes. *Geophysical Journal International*, *166*(3), 1347–1362. doi:
 758 10.1111/j.1365-246X.2006.03071.x
- 759 Bletery, Q., & Nocquet, J. M. (2020). Slip bursts during coalescence of slow slip
 760 events in Cascadia. *Nature Communications*, *11*(1), 1–6. doi: 10.1038/s41467-
 761 -020-15494-4
- 762 Bormann, J. M., Hammond, W. C., Kreemer, C., & Blewitt, G. (2016). Accom-
 763 modulation of missing shear strain in the Central Walker Lane, western North
 764 America: Constraints from dense GPS measurements. *Earth and Planetary*
 765 *Science Letters*, *440*, 169–177. doi: 10.1016/j.epsl.2016.01.015
- 766 Brune, J. N. (1970). Tectonic stress and the spectra of seismic shear waves from
 767 earthquakes. *Journal of Geophysical Research*, *75*(26), 4997–5009. doi: 10
 768 .1029/JB075I026P04997
- 769 Bürgmann, R., Ergintav, S., Segall, P., Hearn, E., McClusky, S., Reilinger, R., ...
 770 Zschau, J. (2002). Time-Dependent Distributed Afterslip on and Deep be-
 771 low the İzmit Earthquake Rupture. *Bulletin of the Seismological Society of*
 772 *America*, *92*, 126–137. doi: 10.1785/0120000833
- 773 Caballero, E., Chounet, A., Duputel, Z., Jara, J., Twardzik, C., & Jolivet, R.
 774 (2021). Seismic and Aseismic Fault Slip During the Initiation Phase of the

- 775 2017 Mw = 6.9 Valparaíso Earthquake. *Geophysical Research Letters*, *48*(6),
776 e2020GL091916. doi: 10.1029/2020GL091916
- 777 Cappa, F., Scuderi, M. M., Collettini, C., Guglielmi, Y., & Avouac, J. P. (2019).
778 Stabilization of fault slip by fluid injection in the laboratory and in situ. *Sci-*
779 *ence Advances*, *5*(3), eaau4065. doi: 10.1126/sciadv.aau4065
- 780 Cattania, C., & Segall, P. (2021). Precursory slow slip and foreshocks on rough
781 faults. *Journal of Geophysical Research: Solid Earth*, e2020JB020430. doi: 10
782 .1029/2020JB020430
- 783 Champenois, J., Baize, S., Vallee, M., Jomard, H., Alvarado, A., Espin, P., . . .
784 Audin, L. (2017). Evidences of Surface Rupture Associated With a
785 Low-Magnitude (Mw 5.0) Shallow Earthquake in the Ecuadorian Andes.
786 *Journal of Geophysical Research: Solid Earth*, *122*(10), 8446–8458. doi:
787 10.1002/2017JB013928
- 788 Cheloni, D., D’Agostino, N., Selvaggi, G., Avallone, A., Fornaro, G., Giuliani,
789 R., . . . Tizzani, P. (2017). Aseismic transient during the 2010-2014
790 seismic swarm: Evidence for longer recurrence of $M \geq 6.5$ earthquakes in
791 the Pollino gap (Southern Italy)? *Scientific Reports*, *7*(1), 1–10. doi:
792 10.1038/s41598-017-00649-z
- 793 Ciardo, F., & Lecampion, B. (2019). Effect of Dilatancy on the Transition From
794 Aseismic to Seismic Slip Due to Fluid Injection in a Fault. *Journal of Geophys-*
795 *ical Research: Solid Earth*, *124*(4), 3724–3743. doi: 10.1029/2018JB016636
- 796 De Barros, L., Cappa, F., Deschamps, A., & Dublanchet, P. (2020). Imbricated
797 Aseismic Slip and Fluid Diffusion Drive a Seismic Swarm in the Corinth Gulf,
798 Greece. *Geophysical Research Letters*, *47*(9). doi: 10.1029/2020GL087142
- 799 Delorey, A. A., van der Elst, N. J., & Johnson, P. A. (2017). Tidal triggering of
800 earthquakes suggests poroelastic behavior on the San Andreas Fault. *Earth*
801 *and Planetary Science Letters*, *460*, 164–170. doi: 10.1016/j.epsl.2016.12.014
- 802 Di Carli, S., François-Holden, C., Peyrat, S., & Madariaga, R. (2010). Dynamic
803 inversion of the 2000 Tottori earthquake based on elliptical subfault ap-
804 proximations. *Journal of Geophysical Research*, *115*(B12), B12328. doi:
805 10.1029/2009JB006358
- 806 Dodge, D. A., Beroza, G. C., & Ellsworth, W. L. (1996). Detailed observations of
807 California foreshock sequences: Implications for the earthquake initiation pro-

- 808 cess. *Journal of Geophysical Research: Solid Earth*, *101*(B10), 22371–22392.
809 doi: 10.1029/96JB02269
- 810 Du, Y., Aydin, A., & Segall, P. (1992). Comparison of various inversion techniques
811 as applied to the determination of a geophysical deformation model for the
812 1983 Borah Peak earthquake. *Bulletin of the Seismological Society of America*,
813 *82*(4), 1840–1866.
- 814 Elliott, J. R., Walters, R. J., England, P. C., Jackson, J. A., Li, Z., & Parsons, B.
815 (2010). Extension on the Tibetan plateau: recent normal faulting measured by
816 InSAR and body wave seismology. *Geophysical Journal International*, *183*(2),
817 503–535. doi: 10.1111/j.1365-246X.2010.04754.x
- 818 Ellsworth, W. L., & Bulut, F. (2018, jun). Nucleation of the 1999 Izmit earthquake
819 by a triggered cascade of foreshocks. *Nature Geoscience*, *11*(7), 531–535. doi:
820 10.1038/s41561-018-0145-1
- 821 Engwirda, D. (2014). *Locally optimal Delaunay-refinement and optimisation-based*
822 *mesh generation* (Doctoral dissertation, University of Sydney). Retrieved from
823 <http://hdl.handle.net/2123/13148>
- 824 Faulds, J., & Henry, C. (2008). Tectonic influences on the spatial and temporal
825 evolution of the Walker Lane: An incipient transform fault along the evolving
826 Pacific - North American plate boundary. *Arizona Geological Society Digest*,
827 *22*, 437–470.
- 828 Floyd, M. A., Walters, R. J., Elliott, J. R., Funning, G. J., Svarc, J. L., Murray,
829 J. R., ... Wright, T. J. (2016, jul). Spatial variations in fault friction re-
830 lated to lithology from rupture and afterslip of the 2014 South Napa, Cali-
831 fornia, earthquake. *Geophysical Research Letters*, *43*(13), 6808–6816. Re-
832 trieved from [https://onlinelibrary.wiley.com/doi/full/10.1002/](https://onlinelibrary.wiley.com/doi/full/10.1002/2016GL069428)
833 2016GL069428[https://onlinelibrary.wiley.com/doi/abs/10.1002/](https://onlinelibrary.wiley.com/doi/abs/10.1002/2016GL069428)
834 2016GL069428[https://agupubs.onlinelibrary.wiley.com/doi/10.1002/](https://agupubs.onlinelibrary.wiley.com/doi/10.1002/2016GL069428)
835 2016GL069428 doi: 10.1002/2016GL069428
- 836 Fukahata, Y., & Wright, T. J. (2008). A non-linear geodetic data inversion using
837 ABIC for slip distribution on a fault with an unknown dip angle. *Geophysical*
838 *Journal International*, *173*(2), 353–364. doi: 10.1111/j.1365-246X.2007.03713
839 .x
- 840 Fukuda, J. (2018). Variability of the Space-Time Evolution of Slow Slip Events Off

- 841 the Boso Peninsula, Central Japan, From 1996 to 2014. *Journal of Geophysical*
 842 *Research: Solid Earth*, *123*(1), 732–760. doi: 10.1002/2017JB014709
- 843 Fukuda, J., & Johnson, K. M. (2008). A fully Bayesian inversion for spatial distri-
 844 bution of fault slip with objective smoothing. *Bulletin of the Seismological So-*
 845 *society of America*, *98*(3), 1128–1146. doi: 10.1785/0120070194
- 846 Fukuda, J., & Johnson, K. M. (2010). Mixed linear-non-linear inversion of crustal
 847 deformation data: Bayesian inference of model, weighting and regularization
 848 parameters. *Geophysical Journal International*, *181*(3), 1441–1458. doi:
 849 10.1111/j.1365-246X.2010.04564.x
- 850 Gavish, M., & Donoho, D. L. (2014). The optimal hard threshold for singular values
 851 is $4/\sqrt{3}$. *IEEE Transactions on Information Theory*, *60*(8), 5040–5053. doi: 10
 852 .1109/TIT.2014.2323359
- 853 Gomberg, J. (2018). Unsettled earthquake nucleation. *Nature Geoscience*, *11*(7),
 854 463–464. doi: 10.1038/s41561-018-0149-x
- 855 Gomberg, J., & Johnson, P. (2005). Dynamic triggering of earthquakes. *Nature*,
 856 *437*(7060), 830. doi: 10.1038/437830a
- 857 González, P. J., Samsonov, S. V., Pepe, S., Tiampo, K. F., Tizzani, P., Casu, F., ...
 858 Sansosti, E. (2013). Magma storage and migration associated with the 2011-
 859 2012 El Hierro eruption: Implications for crustal magmatic systems at oceanic
 860 island volcanoes. *Journal of Geophysical Research: Solid Earth*, *118*(8), 4361–
 861 4377. doi: 10.1002/jgrb.50289
- 862 Grandin, R., Socquet, A., Doin, M.-P., Jacques, E., de Chabalier, J.-B., & King,
 863 G. C. P. (2010). Transient rift opening in response to multiple dike injec-
 864 tions in the Manda Hararo rift (Afar, Ethiopia) imaged by time-dependent
 865 elastic inversion of interferometric synthetic aperture radar data. *Journal of*
 866 *Geophysical Research*, *115*(B9), B09403. doi: 10.1029/2009JB006883
- 867 Gualandi, A., Nichele, C., Serpelloni, E., Chiaraluce, L., Anderlini, L., Latorre, D.,
 868 ... Avouac, J.-P. (2017). Aseismic deformation associated with an earth-
 869 quake swarm in the northern Apennines (Italy). *Geophysical Research Letters*,
 870 *44*(15), 7706–7714. doi: 10.1002/2017GL073687
- 871 Guglielmi, Y., Cappa, F., Avouac, J. P., Henry, P., & Elsworth, D. (2015). Seismic-
 872 ity triggered by fluid injection-induced aseismic slip. *Science*, *348*(6240), 1224–
 873 1226. doi: 10.1126/science.aab0476

- 874 Hamling, I. J., Hreinsdóttir, S., Clark, K., Elliott, J., Liang, C., Fielding, E.,
875 ... Stirling, M. (2017). Complex multifault rupture during the 2016
876 Mw 7.8 Kaikōura earthquake, New Zealand. *Science*, *356*(6334). doi:
877 10.1126/science.aam7194
- 878 Hammond, W. C., & Thatcher, W. (2007). Crustal deformation across the Sierra
879 Nevada, northern Walker Lane, Basin and Range transition, western United
880 States measured with GPS, 2000–2004. *Journal of Geophysical Research: Solid
881 Earth*, *112*(B5), 5411. doi: 10.1029/2006JB004625
- 882 Harris, R. A., & Segall, P. (1987). Detection of a locked zone at depth on the Park-
883 field, California, segment of the San Andreas Fault. *Journal of Geophysical Re-
884 search*, *92*(B8), 7945. doi: 10.1029/JB092iB08p07945
- 885 Hatch, R. L. (2020). *Characterization of Recent Earthquake Sequences and Swarms
886 Within the Walker Lane Tectonic Region* (Doctoral dissertation, University of
887 Nevada, Reno). Retrieved from <http://hdl.handle.net/11714/7569>
- 888 Hatch, R. L., Abercrombie, R. E., Ruhl, C. J., & Smith, K. D. (2018). Earth-
889 quake Interaction, Fault Structure, and Source Properties of a Small Sequence
890 in 2017 near Truckee, California Earthquake Interaction, Fault Structure,
891 and Source Properties of a Small Sequence in 2017 near Truckee. *Bul-
892 letin of the Seismological Society of America*, *108*(5A), 2580–2593. doi:
893 10.1785/0120180089
- 894 Hatch, R. L., Abercrombie, R. E., Ruhl, C. J., & Smith, K. D. (2020). Evidence of
895 Aseismic and Fluid-Driven Processes in a Small Complex Seismic Swarm Near
896 Virginia City, Nevada. *Geophysical Research Letters*, *47*(4), e2019GL085477.
897 doi: 10.1029/2019GL085477
- 898 Hicks, S. P., Okuwaki, R., Steinberg, A., Rychert, C. A., Harmon, N., Abercrombie,
899 R. E., ... Sudhaus, H. (2020). Back-propagating supershear rupture in the
900 2016 Mw 7.1 Romanche transform fault earthquake. *Nature Geoscience*, *13*(9),
901 647–653. doi: 10.1038/s41561-020-0619-9
- 902 Hinz, N., Faulds, J., Moeck, I., Bell, J. W., & Oldow, J. S. (2010). Structural con-
903 trols of three blind geothermal resources at the Hawthorne ammunition depot,
904 West-Central Nevada. *Transactions - Geothermal Resources Council*, *34*,
905 720–725.
- 906 Hirose, H., & Obara, K. (2010). Recurrence behavior of short-term slow slip

- 907 and correlated nonvolcanic tremor episodes in western Shikoku, southwest
 908 Japan. *Journal of Geophysical Research: Solid Earth*, 115(B6), 0–21. doi:
 909 10.1029/2008JB006050
- 910 Houston, H., Delbridge, B. G., Wech, A. G., & Creager, K. C. (2011). Rapid tremor
 911 reversals in Cascadia generated by a weakened plate interface. *Nature Geo-*
 912 *science*, 4(6), 404–409. doi: 10.1038/ngeo1157
- 913 Hussain, E., Hooper, A., Wright, T. J., Walters, R. J., & Bekaert, D. P. (2016).
 914 Interseismic strain accumulation across the central North Anatolian Fault from
 915 iteratively unwrapped InSAR measurements. *Journal of Geophysical Research:*
 916 *Solid Earth*, 121(12), 9000–9019. doi: 10.1002/2016JB013108
- 917 Ichinose, G. A., Anderson, J. G., Smith, K. D., & Zeng, Y. (2003). Source Param-
 918 eters of Eastern California and Western Nevada Earthquakes from Regional
 919 Moment Tensor Inversion. *Bulletin of the Seismological Society of America*,
 920 93(1), 61–84. doi: 10.1785/0120020063
- 921 Ingleby, T., Wright, T. J., Hooper, A., Craig, T. J., & Elliott, J. R. (2020, feb).
 922 Constraints on the Geometry and Frictional Properties of the Main Himalayan
 923 Thrust Using Coseismic, Postseismic, and Interseismic Deformation in Nepal.
 924 *Journal of Geophysical Research: Solid Earth*, 125(2), e2019JB019201. Re-
 925 trieved from [https://onlinelibrary.wiley.com/doi/full/10.1029/](https://onlinelibrary.wiley.com/doi/full/10.1029/2019JB019201)
 926 [2019JB019201](https://onlinelibrary.wiley.com/doi/abs/10.1029/2019JB019201)[https://onlinelibrary.wiley.com/doi/abs/10.1029/](https://onlinelibrary.wiley.com/doi/abs/10.1029/2019JB019201)
 927 [https://agupubs.onlinelibrary.wiley.com/doi/10.1029/](https://agupubs.onlinelibrary.wiley.com/doi/10.1029/2019JB019201)
 928 [2019JB019201](https://agupubs.onlinelibrary.wiley.com/doi/10.1029/2019JB019201) doi: 10.1029/2019JB019201
- 929 Jiang, Y., & González, P. J. (2020). Bayesian Inversion of Wrapped Satellite
 930 Interferometric Phase to Estimate Fault and Volcano Surface Ground Defor-
 931 mation Models. *Journal of Geophysical Research: Solid Earth*, 125(5). doi:
 932 10.1029/2019JB018313
- 933 Jiang, Y., & González, P. J. (2021). High-resolution spatio-temporal fault slip using
 934 InSAR observations: insights on seismic and aseismic slip during a shallow
 935 crust earthquake swarm. In *EGU General Assembly Conference Abstracts*. doi:
 936 10.5194/egusphere-egu21-6280
- 937 Jiang, Y., González, P. J., & Bürgmann, R. (2021). Subduction earthquakes con-
 938 trolled by incoming plate geometry: The 2020 $M > 7.5$ Shumagin, Alaska,
 939 earthquake doublet. *EarthArXiv*. doi: 10.31223/X5H91J

- 940 Johanson, I. A., & Bürgmann, R. (2005). Creep and quakes on the northern tran-
 941 sition zone of the San Andreas fault from GPS and InSAR data. *Geophysical*
 942 *Research Letters*, *32*(14), 1–5. doi: 10.1029/2005GL023150
- 943 Johnson, K. M., Fukuda, J., & Segall, P. (2012). Challenging the rate-state as-
 944 perity model: Afterslip following the 2011 M9 Tohoku-oki, Japan, earth-
 945 quake. *Geophysical Research Letters*, *39*(20), 2012GL052901. doi:
 946 10.1029/2012GL052901
- 947 Jolivet, R., Lasserre, C., Doin, M. P., Guillaso, S., Peltzer, G., Dailu, R., . . . Xu, X.
 948 (2012). Shallow creep on the Haiyuan Fault (Gansu, China) revealed by SAR
 949 Interferometry. *Journal of Geophysical Research: Solid Earth*, *117*(B6), 6401.
 950 doi: 10.1029/2011JB008732
- 951 Kampes, B., Hanssen, R., & Perski, Z. (2003). Radar interferometry with public do-
 952 main tools. *Proc. of FRINGE 2003 Workshop*.
- 953 Kaneko, Y., & Shearer, P. M. (2014). Seismic source spectra and estimated stress
 954 drop derived from cohesive-zone models of circular subshear rupture. *Geophys-*
 955 *ical Journal International*, *197*(2), 1002–1015. doi: 10.1093/gji/ggu030
- 956 Ke, C.-Y., McLaskey, G. C., & Kammer, D. S. (2020). The Earthquake Arrest Zone.
 957 *Geophysical Journal International*. doi: 10.1093/gji/ggaa386
- 958 Khoshmanesh, M., Shirzaei, M., & Nadeau, R. M. (2015). Time-dependent model
 959 of aseismic slip on the central San Andreas Fault from InSAR time series and
 960 repeating earthquakes. *Journal of Geophysical Research: Solid Earth*, *120*(9),
 961 6658–6679. doi: 10.1002/2015JB012039
- 962 King, G. C. P., Stein, R. S., & Lin, J. (1994, jun). Static stress changes and the trig-
 963 gering of earthquakes. *Bulletin of the Seismological Society of America*, *84*(3),
 964 935-953.
- 965 Klein, E., Duputel, Z., Zigone, D., Vigny, C., Boy, J.-P., Doubre, C., & Meneses,
 966 G. (2018). Deep transient slow slip detected by survey gps in the region of
 967 atacama, chile. *Geophysical Research Letters*, *45*(22), 12,263-12,273. doi:
 968 10.1029/2018GL080613
- 969 Kreemer, C., Blewitt, G., & Hammond, W. C. (2009). Geodetic constraints on
 970 contemporary deformation in the northern Walker Lane: 2. Velocity and
 971 strain rate tensor analysis. In *Late Cenozoic Structure and Evolution of the*
 972 *Great Basin-Sierra Nevada Transition*. Geological Society of America. doi:

- 973 10.1130/2009.2447(02)
- 974 Kreemer, C., Blewitt, G., & Klein, E. C. (2014). A geodetic plate motion and Global
975 Strain Rate Model. *Geochemistry, Geophysics, Geosystems*, *15*(10), 3849–3889.
976 doi: 10.1002/2014GC005407
- 977 Kyriakopoulos, C., Chini, M., Bignami, C., Stramondo, S., Ganas, A., Kolligri, M.,
978 & Moshou, A. (2013). Monthly migration of a tectonic seismic swarm detected
979 by DInSAR: Southwest Peloponnese, Greece. *Geophysical Journal Interna-*
980 *tional*, *194*(3), 1302–1309. doi: 10.1093/gji/ggt196
- 981 Lambert, V., Lapusta, N., & Perry, S. (2021). Propagation of large earthquakes as
982 self-healing pulses or mild cracks. *Nature*, *591*(7849), 252–258. doi: 10.1038/
983 s41586-021-03248-1
- 984 Lange, R. A., & Carmichael, I. S. E. (1996). The Aurora volcanic field, California-
985 Nevada: oxygen fugacity constraints on the development of andesitic
986 magma. *Contributions to Mineralogy and Petrology*, *125*(2), 167–185. doi:
987 10.1007/s004100050214
- 988 Latour, S., Schubnel, A., Nielsen, S., Madariaga, R., & Vinciguerra, S. (2013, oct).
989 Characterization of nucleation during laboratory earthquakes. *Geophysical Re-*
990 *search Letters*, *40*(19), 5064–5069. doi: 10.1002/GRL.50974
- 991 Liu, Y., McGuire, J. J., & Behn, M. D. (2020). Aseismic transient slip on the Go-
992 far transform fault, East Pacific Rise. *Proceedings of the National Academy of*
993 *Sciences of the United States of America*, *117*(19), 10188–10194. doi: 10.1073/
994 pnas.1913625117
- 995 Lohman, R. B., & McGuire, J. J. (2007). Earthquake swarms driven by aseismic
996 creep in the Salton Trough, California. *Journal of Geophysical Research: Solid*
997 *Earth*, *112*(4). doi: 10.1029/2006JB004596
- 998 Luo, Y., & Liu, Z. (2019). Rate-and-State Model Casts New Insight into Episodic
999 Tremor and Slow-slip Variability in Cascadia. *Geophysical Research Letters*,
1000 *46*(12), 6352–6362. doi: 10.1029/2019GL082694
- 1001 Madariaga, R. (1976). Dynamics of an expanding circular fault. *Bulletin of the Seis-*
1002 *mological Society of America*, *66*(3), 639–666.
- 1003 Mai, P. M., & Beroza, G. C. (2002). A spatial random field model to characterize
1004 complexity in earthquake slip. *Journal of Geophysical Research: Solid Earth*,
1005 *107*(B11), ESE 10–1–ESE 10–21. doi: 10.1029/2001jb000588

- 1006 Mai, P. M., & Thingbaijam, K. K. (2014). SRCMOD: An online database of finite-
 1007 fault rupture models. *Seismological Research Letters*, *85*(6), 1348–1357. doi:
 1008 10.1785/0220140077
- 1009 Marone, C., & Richardson, E. (2006). Do earthquakes rupture piece by piece or all
 1010 together? *Science*, *313*(5794), 1748–1749. doi: 10.1126/science.1131296
- 1011 Matthews, M. V., & Segall, P. (1993). Estimation of depth-dependent fault slip
 1012 from measured surface deformation with application to the 1906 San Francisco
 1013 earthquake. *Journal of Geophysical Research*, *98*(B7), 12153–12163. doi:
 1014 10.1029/93jb00440
- 1015 Mesimeri, M., & Karakostas, V. (2018). Repeating earthquakes in western Corinth
 1016 Gulf (Greece): Implications for aseismic slip near locked faults. *Geophysical*
 1017 *Journal International*, *215*(1), 659–676. doi: 10.1093/gji/ggy301
- 1018 Michel, S., Gualandi, A., & Avouac, J. P. (2019). Similar scaling laws for earth-
 1019 quakes and Cascadia slow-slip events. *Nature*, *574*(7779), 522–526. doi: 10
 1020 .1038/s41586-019-1673-6
- 1021 Minson, S. E., Simons, M., & Beck, J. L. (2013). Bayesian inversion for finite fault
 1022 earthquake source models I—theory and algorithm. *Geophysical Journal Inter-*
 1023 *national*, *194*(3), 1701–1726. doi: 10.1093/gji/ggt180
- 1024 Mori, J. (1996). Rupture directivity and slip distribution of the M 4.3 foreshock to
 1025 the 1992 Joshua Tree earthquake, Southern California. *Bulletin of the Seismo-*
 1026 *logical Society of America*, *86*(3), 805–810. doi: 10.1785/BSSA0860030805
- 1027 Nadeau, R. M., & McEvilly, T. V. (1999). Fault slip rates at depth from recurrence
 1028 intervals of repeating microearthquakes. *Science*, *285*(5428), 718–721. doi: 10
 1029 .1126/science.285.5428.718
- 1030 Nissen, E., Ghorashi, M., Jackson, J., Parsons, B., & Talebian, M. (2007). The
 1031 2005 Qeshm Island earthquake (Iran) - A link between buried reverse faulting
 1032 and surface folding in the Zagros Simply Folded Belt? *Geophysical Journal*
 1033 *International*, *171*(1), 326–338. doi: 10.1111/j.1365-246X.2007.03514.x
- 1034 Ohnaka, M., & Kuwahara, Y. (1990). Characteristic features of local breakdown
 1035 near a crack-tip in the transition zone from nucleation to unstable rup-
 1036 ture during stick-slip shear failure. *Tectonophysics*, *175*(1), 197–220. doi:
 1037 [https://doi.org/10.1016/0040-1951\(90\)90138-X](https://doi.org/10.1016/0040-1951(90)90138-X)
- 1038 Ozawa, S., Yarai, H., & Kobayashi, T. (2019). Recovery of the recurrence interval of

- 1039 Boso slow slip events in Japan. *Earth, Planets and Space*, *71*(1), 1–8. doi: 10
 1040 .1186/s40623-019-1058-y
- 1041 Parotidis, M., Rothert, E., & Shapiro, S. A. (2003). Pore-pressure diffu-
 1042 sion: A possible triggering mechanism for the earthquake swarms 2000 in
 1043 Vogtland/NW-Bohemia, central Europe. *Geophysical Research Letters*, *30*(20),
 1044 2003GL018110. doi: 10.1029/2003GL018110
- 1045 Passarelli, L., Rivalta, E., Jónsson, S., Hensch, M., Metzger, S., Jakobsdóttir, S. S.,
 1046 ... Dahm, T. (2018). Scaling and spatial complementarity of tectonic
 1047 earthquake swarms. *Earth and Planetary Science Letters*, *482*, 62–70. doi:
 1048 10.1016/j.epsl.2017.10.052
- 1049 Pritchard, M. E., & Simons, M. (2006). An aseismic slip pulse in northern Chile
 1050 and along-strike variations in seismogenic behavior. *Journal of Geophysical Re-
 1051 search: Solid Earth*, *111*(8). doi: 10.1029/2006JB004258
- 1052 Radiguet, M., Cotton, F., Vergnolle, M., Campillo, M., Valette, B., Kostoglodov, V.,
 1053 & Cotte, N. (2011). Spatial and temporal evolution of a long term slow slip
 1054 event: the 2006 Guerrero Slow Slip Event. *Geophysical Journal International*,
 1055 *184*(2), 816–828. doi: 10.1111/j.1365-246X.2010.04866.x
- 1056 Radiguet, M., Perfettini, H., Cotte, N., Gualandi, A., Valette, B., Kostoglodov, V.,
 1057 ... Campillo, M. (2016). Triggering of the 2014 Mw7.3 Papanao earthquake
 1058 by a slow slip event in Guerrero, Mexico. *Nature Geoscience* *2016 9:11*, *9*(11),
 1059 829–833. doi: 10.1038/ngeo2817
- 1060 Ragon, T., Sladen, A., & Simons, M. (2018). Accounting for uncertain fault geome-
 1061 try in earthquake source inversions – I: theory and simplified application. *Geo-
 1062 physical Journal International*, *214*(2), 1174–1190. doi: 10.1093/gji/ggy187
- 1063 Romanet, P., Bhat, H. S., Jolivet, R., & Madariaga, R. (2018). Fast and Slow Slip
 1064 Events Emerge Due to Fault Geometrical Complexity. *Geophysical Research
 1065 Letters*, *45*(10), 4809–4819. doi: 10.1029/2018GL077579
- 1066 Rousset, B., Fu, Y., Bartlow, N., & Bürgmann, R. (2019). Weeks-Long and Years-
 1067 Long Slow Slip and Tectonic Tremor Episodes on the South Central Alaska
 1068 Megathrust. *Journal of Geophysical Research: Solid Earth*, *124*(12), 13392–
 1069 13403. doi: 10.1029/2019JB018724
- 1070 Ruhl, C. J., Abercrombie, R. E., & Smith, K. D. (2017). Spatiotemporal Varia-
 1071 tion of Stress Drop During the 2008 Mogul, Nevada, Earthquake Swarm. *Jour-*

- 1072 *nal of Geophysical Research: Solid Earth*, 122(10), 8163–8180. doi: 10.1002/
1073 2017JB014601
- 1074 Ruhl, C. J., Abercrombie, R. E., Smith, K. D., & Zaliapin, I. (2016). Complex
1075 spatiotemporal evolution of the 2008 Mw 4.9 Mogul earthquake swarm (Reno,
1076 Nevada): Interplay of fluid and faulting. *Journal of Geophysical Research:*
1077 *Solid Earth*, 121(11), 8196–8216. doi: 10.1002/2016JB013399
- 1078 Ruhl, C. J., Morton, E. A., Bormann, J. M., Hatch-Ibarra, R., Ichinose, G., &
1079 Smith, K. D. (2021). Complex Fault Geometry of the 2020 Mww 6.5 Monte
1080 Cristo Range, Nevada, Earthquake Sequence. *Seismological Research Letters*,
1081 92(3), 1876–1890. doi: 10.1785/0220200345
- 1082 Salman, R., Hill, E. M., Feng, L., Lindsey, E. O., Mele Veedu, D., Barbot, S., ...
1083 Natawidjaja, D. H. (2017). Piecemeal Rupture of the Mentawai Patch, Suma-
1084 tra: The 2008 Mw 7.2 North Pagai Earthquake Sequence. *Journal of Geophys-*
1085 *ical Research: Solid Earth*, 122(11), 9404–9419. doi: 10.1002/2017JB014341
- 1086 Samsonov, S., & D’Oreye, N. (2012). Multidimensional time-series analysis of
1087 ground deformation from multiple InSAR data sets applied to Virunga Vol-
1088 canic Province. *Geophysical Journal International*, 191(3), 1095–1108. doi:
1089 10.1111/j.1365-246X.2012.05669.x
- 1090 Schmidt, D. A., Bürgmann, R., Nadeau, R. M., & D’Alessio, M. (2005). Distribution
1091 of aseismic slip rate on the Hayward fault inferred from seismic and geode-
1092 tic data. *Journal of Geophysical Research: Solid Earth*, 110(B8), 1–15. doi:
1093 10.1029/2004JB003397
- 1094 Scott, C., Bunds, M., Shirzaei, M., & Toke, N. (2020). Creep Along the Central San
1095 Andreas Fault From Surface Fractures, Topographic Differencing, and InSAR.
1096 *Journal of Geophysical Research: Solid Earth*, 125(10), e2020JB019762. doi:
1097 10.1029/2020JB019762
- 1098 Segall, P., & Rice, J. R. (1995). Dilatancy, compaction, and slip instability of a
1099 fluid-infiltrated fault. *Journal of Geophysical Research: Solid Earth*, 100(B11),
1100 22155–22171. doi: 10.1029/95JB02403
- 1101 Segall, P., Rubin, A. M., Bradley, A. M., & Rice, J. R. (2010). Dilatant strength-
1102 ening as a mechanism for slow slip events. *Journal of Geophysical Research*,
1103 115(B12), B12305. doi: 10.1029/2010JB007449
- 1104 Shearer, P. M., Prieto, G. A., & Hauksson, E. (2006). Comprehensive analysis of

- 1105 earthquake source spectra in southern California. *Journal of Geophysical Re-*
 1106 *search: Solid Earth*, 111(B6), 6303. doi: 10.1029/2005JB003979
- 1107 Shen, Z. K., Sun, J., Zhang, P., Wan, Y., Wang, M., Bürgmann, R., ... Wang,
 1108 Q. (2009). Slip maxima at fault junctions and rupturing of barriers during
 1109 the 2008 Wenchuan earthquake. *Nature Geoscience*, 2(10), 718–724. doi:
 1110 10.1038/ngeo636
- 1111 Smith, K., Johnson, C., Davies, J., Agbaje, T., Knezevic Antonijevec, S., & Kent, G.
 1112 (2011). The 2011 Hawthorne, Nevada, Earthquake Sequence: Shallow Normal
 1113 Faulting. In *AGU Fall Meeting* (pp. S53B–2284).
- 1114 Song, X., Jiang, Y., Shan, X., Gong, W., & Qu, C. (2019). A Fine Velocity and
 1115 Strain Rate Field of Present-Day Crustal Motion of the Northeastern Tibetan
 1116 Plateau Inverted Jointly by InSAR and GPS. *Remote Sensing 2019, Vol. 11,*
 1117 *Page 435, 11(4)*, 435. doi: 10.3390/RS11040435
- 1118 Stein, S., & Gordon, R. G. (1984). Statistical tests of additional plate boundaries
 1119 from plate motion inversions. *Earth and Planetary Science Letters*, 69(2), 401–
 1120 412. doi: 10.1016/0012-821X(84)90198-5
- 1121 Sun, J., Johnson, K. M., Cao, Z., Shen, Z., Bürgmann, R., & Xu, X. (2011). Me-
 1122 chanical constraints on inversion of coseismic geodetic data for fault slip and
 1123 geometry: Example from InSAR observation of the 6 October 2008 Mw 6.3
 1124 Dangxiong-Yangyi (Tibet) earthquake. *Journal of Geophysical Research*,
 1125 116(B1), B01406. doi: 10.1029/2010JB007849
- 1126 Takenaka, H., & Fujii, Y. (2008). A compact representation of spatio-temporal slip
 1127 distribution on a rupturing fault. *Journal of Seismology*, 12, 281–293. doi: 10
 1128 .1007/s10950-007-9087-6
- 1129 Taymaz, T., Wright, T. J., Yolsal, S., Tan, O., Fielding, E., & Seyitoğlu, G. (2007).
 1130 Source characteristics of the 6 June 2000 Orta-Çankiri (central Turkey) earth-
 1131 quake: A synthesis of seismological, geological and geodetic (InSAR) obser-
 1132 vations, and internal deformation of the Anatolian plate. *Geological Society*
 1133 *Special Publication*, 291(1), 259–290. doi: 10.1144/SP291.12
- 1134 Thomas, M. Y., Avouac, J.-P., Champenois, J., Lee, J.-C., Kuo, L.-C., Thomas,
 1135 M. Y., ... Kuo, L.-C. (2014). Spatiotemporal evolution of seismic and aseis-
 1136 mic slip on the Longitudinal Valley Fault, Taiwan. *Journal of Geophysical*
 1137 *Research: Solid Earth*, 119(6), 5114–5139. doi: 10.1002/2013JB010603

- 1138 Tridon, M., Cayol, V., Froger, J., Augier, A., & Bachèlery, P. (2016). Inversion of co-
 1139 eval shear and normal stress of Piton de la Fournaise flank displacement. *Journal of Geophysical Research: Solid Earth*, *121*(11), 7846–7866. doi: 10.1002/
 1140 2016JB013330
 1141
- 1142 Tsang, L. L. H., Hill, E. M., Barbot, S., Qiu, Q., Feng, L., Hermawan, I., ... Natawidjaja, D. H. (2016). Afterslip following the 2007 Mw 8.4 Bengkulu earthquake
 1143 in Sumatra loaded the 2010 Mw 7.8 Mentawai tsunami earthquake rupture
 1144 zone. *Journal of Geophysical Research: Solid Earth*, *121*(12), 9034–9049. doi:
 1145 10.1002/2016JB013432
 1146
- 1147 Turner, R. C., Nadeau, R. M., & Bürgmann, R. (2013). Aseismic slip and fault in-
 1148 teraction from repeating earthquakes in the Loma Prieta aftershock zone. *Geo-
 1149 physical Research Letters*, *40*(6), 1079–1083. doi: 10.1002/grl.50212
- 1150 Uchide, T., Shearer, P. M., & Imanishi, K. (2014). Stress drop variations among
 1151 small earthquakes before the 2011 Tohoku-oki, Japan, earthquake and impli-
 1152 cations for the main shock. *Journal of Geophysical Research: Solid Earth*,
 1153 *119*(9), 7164–7174. doi: 10.1002/2014JB010943
- 1154 Villegas-Lanza, J. C., Nocquet, J. M., Rolandone, F., Vallee, M., Tavera, H., Bon-
 1155 doux, F., ... Chlieh, M. (2016). A mixed seismic-aseismic stress release
 1156 episode in the Andean subduction zone. *Nature Geoscience*, *9*(2), 150–154.
 1157 doi: 10.1038/ngeo2620
- 1158 Wallace, L. M. (2020). Slow slip events in new zealand. *Annual Review of Earth
 1159 and Planetary Sciences*, *48*(1), 175-203. doi: 10.1146/annurev-earth-071719
 1160 -055104
- 1161 Wallace, L. M., Beavan, J., Bannister, S., & Williams, C. (2012). Simultaneous long-
 1162 term and short-term slow slip events at the Hikurangi subduction margin, New
 1163 Zealand: Implications for processes that control slow slip event occurrence,
 1164 duration, and migration. *Journal of Geophysical Research B: Solid Earth*,
 1165 *117*(11). doi: 10.1029/2012JB009489
- 1166 Walters, R. J., Elliott, J. R., D’Agostino, N., England, P. C., Hunstad, I., Jackson,
 1167 J. A., ... Roberts Edinburgh, G. (2009). The 2009 L’Aquila earthquake
 1168 (central Italy): A source mechanism and implications for seismic hazard. *Geo-
 1169 physical Research Letters*, *36*(17). doi: 10.1029/2009GL039337
- 1170 Wech, A. G., Creager, K. C., & Melbourne, T. I. (2009). Seismic and geodetic con-

- 1171 strains on Cascadia slow slip. *Journal of Geophysical Research: Solid Earth*,
1172 114(10). doi: 10.1029/2008JB006090
- 1173 Werner, C. (2000). GAMMA SAR and interferometric processing software. *Proceed-*
1174 *ings of ERS-Envisat Symposium ; 16-20 October, Gothenburg, Sweden, 2000.*
- 1175 Wesnousky, S. (2005). Active faulting in the walker lane. *Tectonics*, 24(3). doi: 10
1176 .1029/2004TC001645
- 1177 Wesnousky, S. (2021). *The Walker Lane: A Potential Target for SCEC Studies?* —
1178 *Southern California Earthquake Center.* Retrieved 2022-01-07, from [https://](https://www.scec.org/article/731)
1179 www.scec.org/article/731
- 1180 Wicks, C., Thelen, W., Weaver, C., Gomberg, J., Rohay, A., & Bodin, P. (2011).
1181 InSAR observations of aseismic slip associated with an earthquake swarm in
1182 the Columbia River flood basalts. *Journal of Geophysical Research*, 116(B12),
1183 B12304. doi: 10.1029/2011JB008433
- 1184 Xu, W., Bürgmann, R., & Li, Z. (2016). An improved geodetic source model for the
1185 1999 Mw 6.3 Chamoli earthquake, India. *Geophysical Journal International*,
1186 205(1), 236–242. doi: 10.1093/gji/ggw016
- 1187 Yamashita, Y., Yakiwara, H., Asano, Y., Shimizu, H., Uchida, K., Hirano, S., ...
1188 Obara, K. (2015). Migrating tremor off southern Kyushu as evidence for
1189 slow slip of a shallow subduction interface. *Science*, 348(6235), 676–679. doi:
1190 10.1126/science.aaa4242
- 1191 Zha, X., Jia, Z., Dai, Z., & Lu, Z. (2019). The cause of the 2011 Hawthorne
1192 (Nevada) earthquake swarm constrained by seismic and InSAR methods.
1193 *Journal of Geodesy*, 93(6), 899–909. doi: 10.1007/s00190-018-1212-5

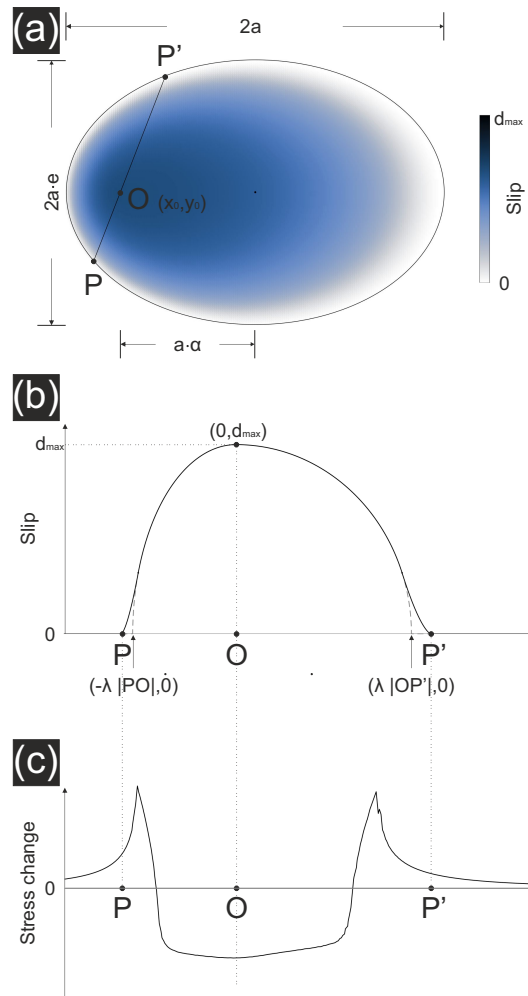


Figure 1. Parameters of the proposed slip model. Image (a) shows the 2d slip distribution, with an elliptical shape. The slip and stress changes along profile POP' are presented in images (b)-(c).

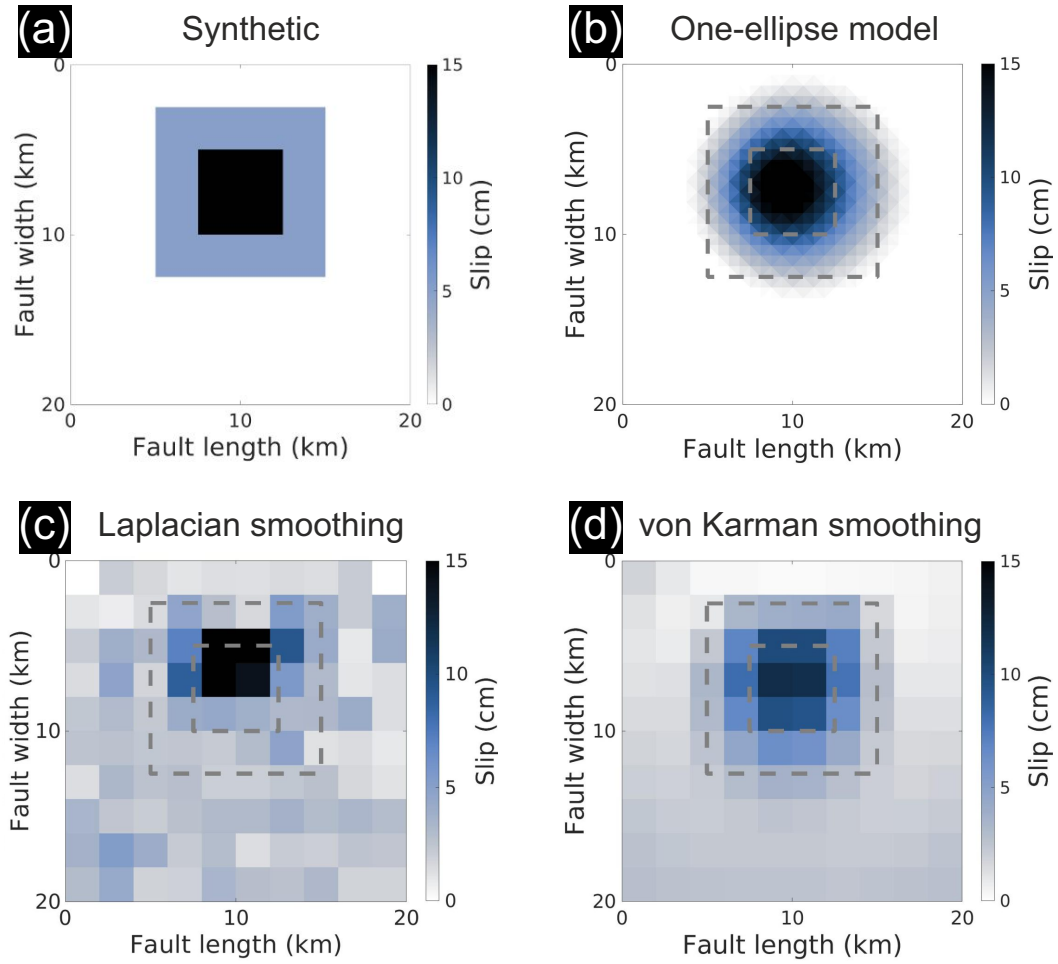


Figure 2. Synthetic and modeled fault slip distribution for a synthetic case. Image (a) shows the synthetic non-uniform slip distribution on a simulated fault plane. The black area is a $5\text{km} \times 5\text{km}$ region with 15cm down-dip slip. The blue area is a $10\text{km} \times 10\text{km}$ region with 5cm down-dip slip. No slip occurs in the white area. Images (b)-(d) are the inverted fault slip distribution based on the optimal model with maximum likelihood estimated by one-ellipse model (GICMo), Laplacian smoothing and von Karman smoothing (slipBERI). The dashed line in image (b)-(d) indicate the boundary of various slipping area in image (a).

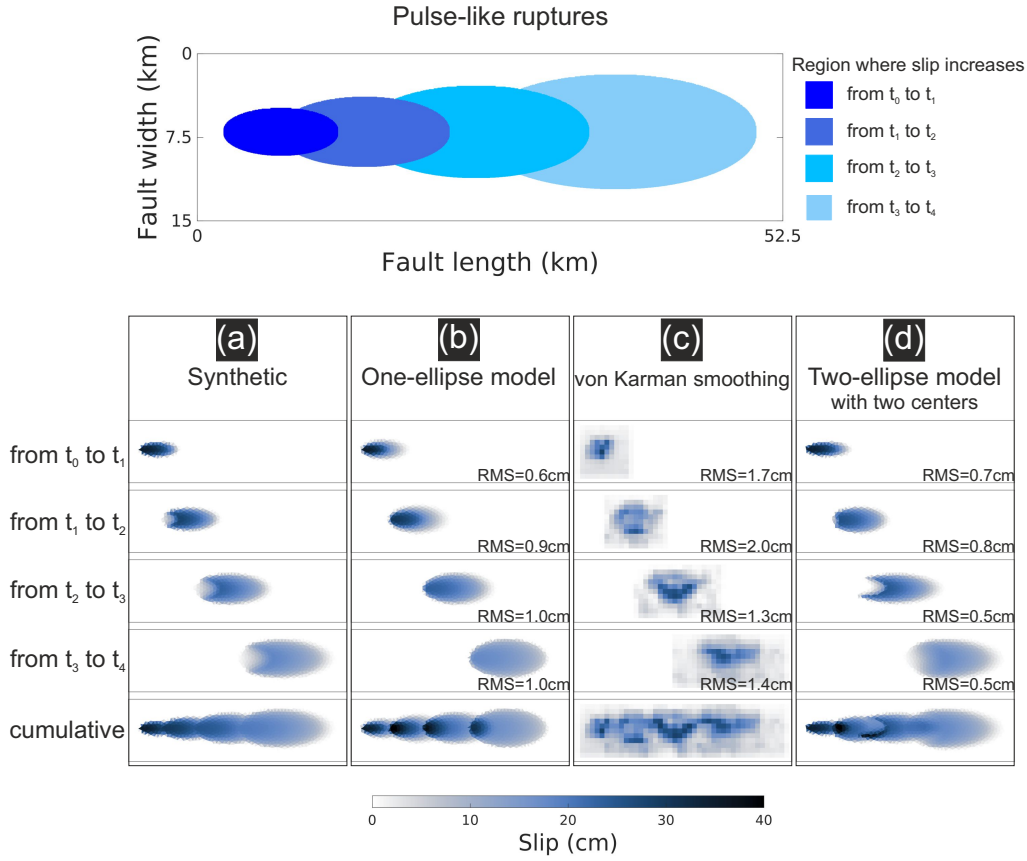


Figure 3. Synthetic and modeled fault slip distributions for synthetic case 2 (pulse-like ruptures). The top image is the conceptual diagram representing the growing cracks with the overlapping relationship. Images in column (a) show the synthetic slip increments. Images in columns (b)-(d) show the modeled slip distribution with various inversion methods: one-ellipse model (b), von Karman smoothing (c), and two-ellipse model with different centers (d), and the RMS of the slip residuals are shown at the bottom right.

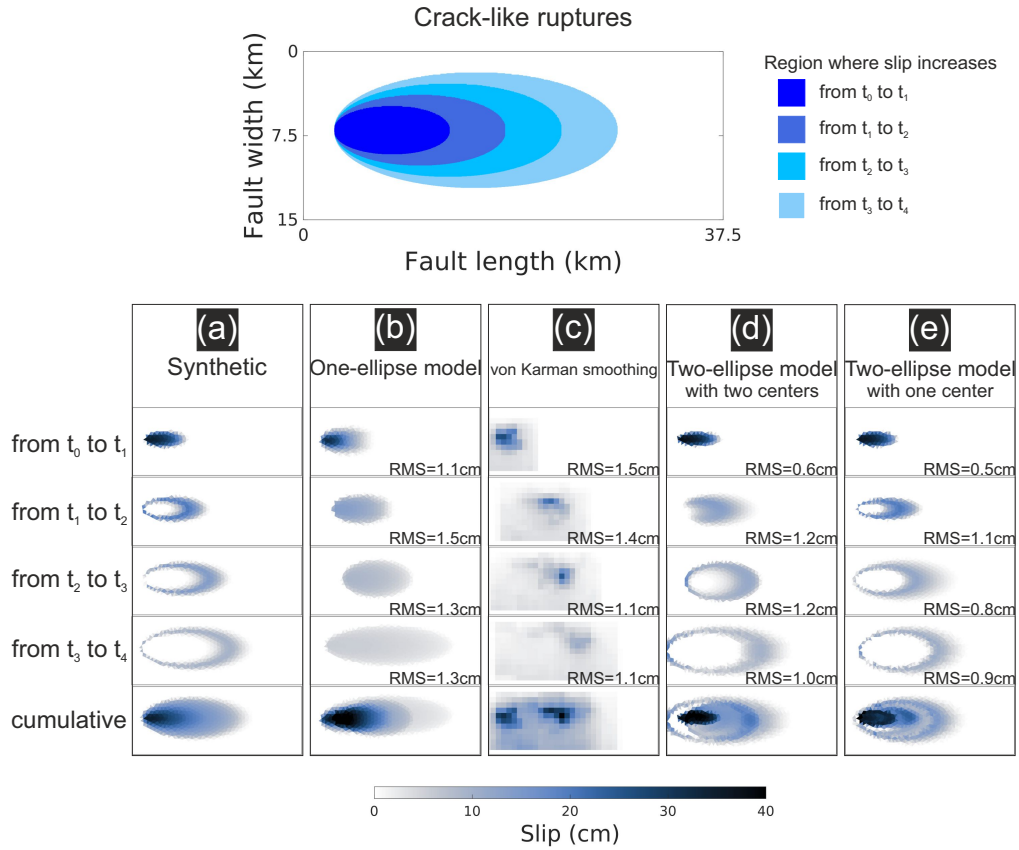


Figure 4. Synthetic and modeled fault slip distribution for synthetic case 2 (crack-like ruptures). The top image is the conceptual diagram presenting the growing cracks with the containing relationship. Images in column (a) show the synthetic slip increments. Images in columns (b)-(e) show the modeled slip distribution with various inversion methods: one-ellipse model (b), von Karman smoothing (c), two-ellipse model with different centers (d) and with the same center (e), and the RMS of the slip residuals are shown at the bottom right.

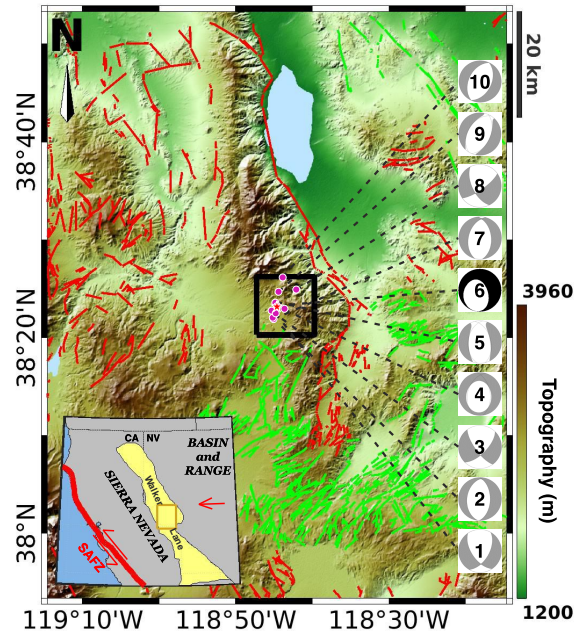


Figure 5. Tectonic settings for the 2011 Hawthorne seismic swarm. Image (a) shows the structural geologic environment of Walker Lane, located between the Sierra Nevada microplate and Basin and Range Province. It accommodates relative motion between the Pacific and North America. The brown rectangular box is the boundary of image (b), the central segment of Walker Lane. Image (b) shows the detailed tectonic settings for the 2011 Hawthorne seismic swarm, with topography as the base map. Normal and strike-slip faults are plotted as red and green lines. The beach balls on the right show the focal mechanism solutions provided by the Nevada Seismological Laboratory (Ichinose et al., 2003). Beach ball No.6 in black is the event with the largest magnitude, M4.6. Abbreviation: SAFZ, San Andreas Fault Zone

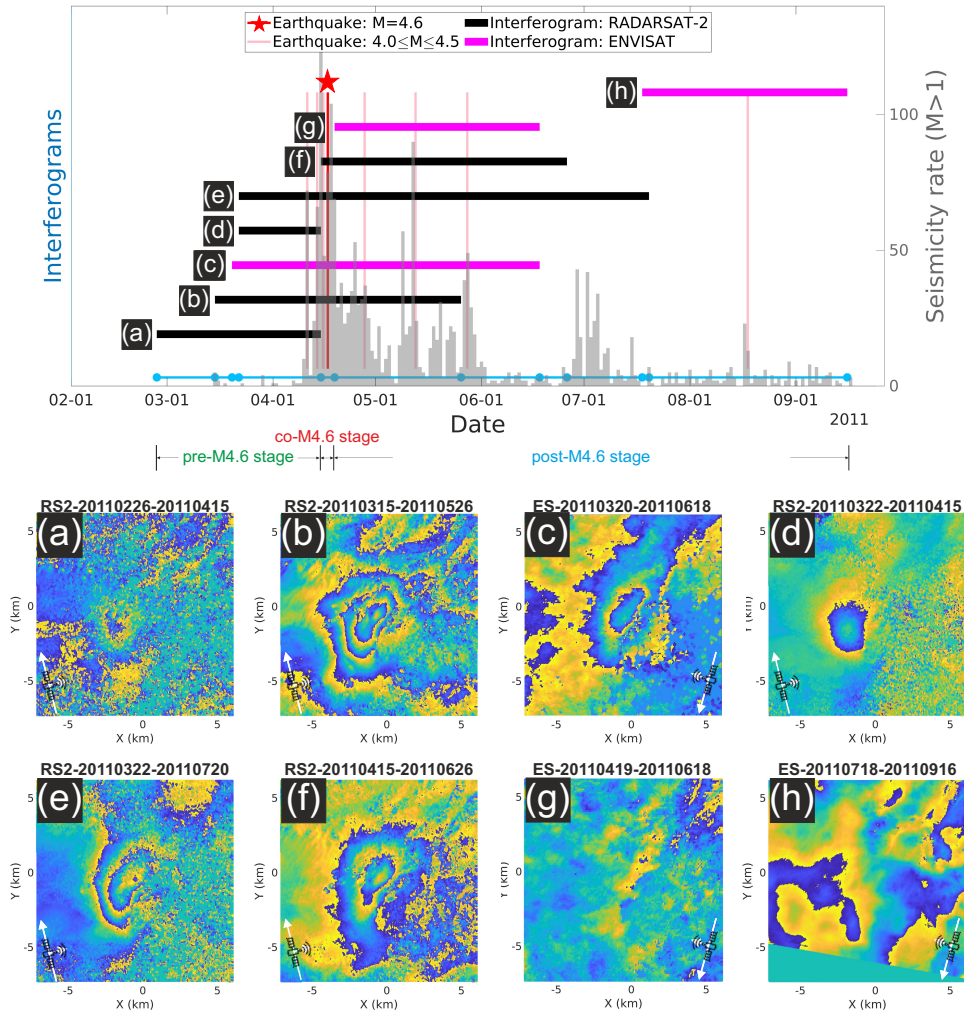


Figure 6. Surface displacement observations for the 2011 Hawthorne seismic swarm. In this research, the 2011 Hawthorne seismic swarm is divided into 3 stages with respect to the largest event, M4.6 on April 17 2011 (red star in the top image): pre-, co- and post-M4.6 event. The top image shows the time coverage of the interferograms (horizontal lines) over $M \geq 4$ events (vertical lines). Out of 8 interferograms (a)-(h), 5 are from RADARSAT-2 (black lines) and 3 from ENVISAT (magenta lines). For the blue line at the bottom, dots infer the 11 dates for the image sensing time in the interferograms. Images (a)-(g) show the observed wrapped phases of the interferograms capturing the surface deformation of the seismic swarm, while no clear deformation signal is detectable in image (h). The spatial reference point is $[38.3875^\circ\text{N}, 118.725^\circ\text{W}]$.

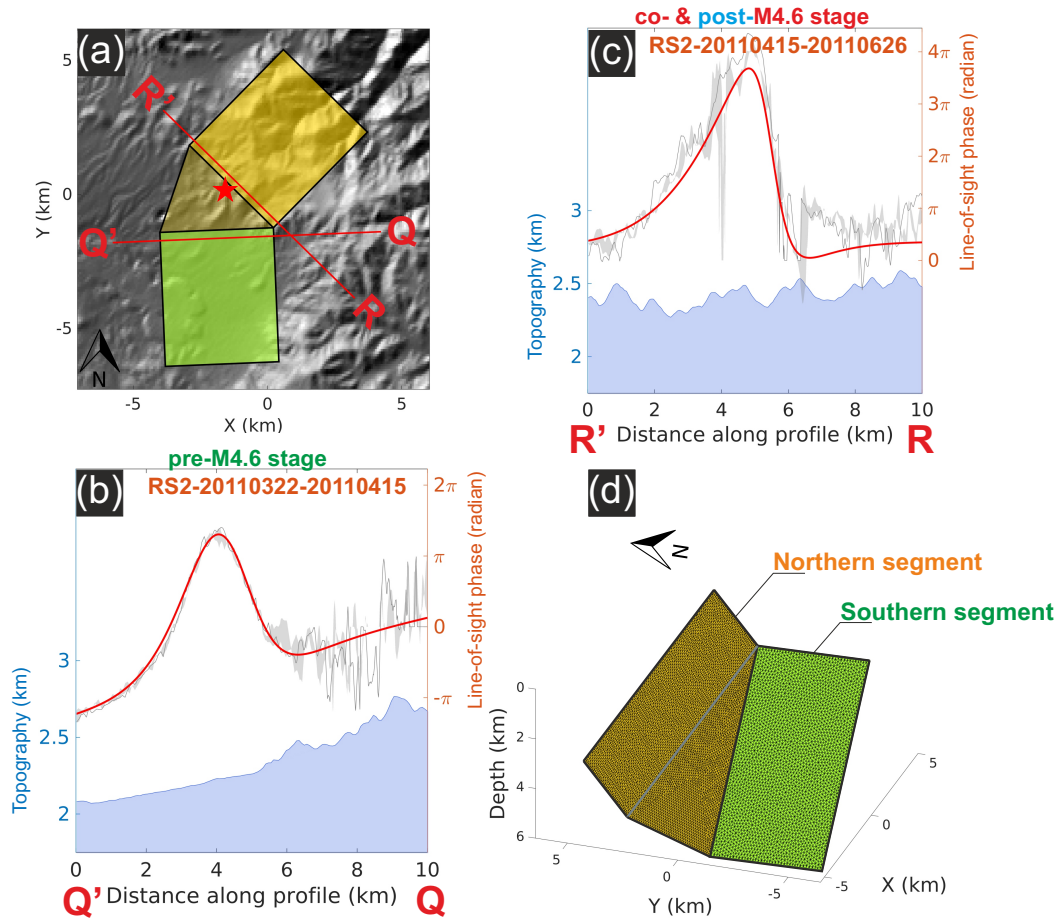


Figure 7. Fault geometry for the 2011 Hawthorne seismic swarm. Image (a) indicates the fault plane with uniform slip retrieved by WGBIS (Jiang & González, 2020) from the wrapped interferograms, and the modeled phase and phase residuals are shown in Figure S8. In image (a), the green rectangle indicates the southern subfault which is active during the pre-M4.6 stage, retrieved from RADARSAT-2 interferogram 2011/03/22-2011/04/15; yellow rectangle indicates the northern subfault which is active during the co- and post-M4.6 stages, retrieved from the RADARSAT-2 interferogram 2011/04/15-2011/06/26, and the yellow triangle indicates the joint fault connecting two rectangle subfaults. Profiles QQ' and RR' are perpendicular to two rectangle subfaults and the red star indicates the hypocentre of the M4.6 event. Images (b) and (c) show the observed and modeled phase along profiles QQ' and RR'. Image (d) shows the discretization of the fault geometry in image (a), where the triangular mesh is generated by FaultResampler (Barnhart & Lohman, 2010) and mesh2d (Engwirda, 2014).

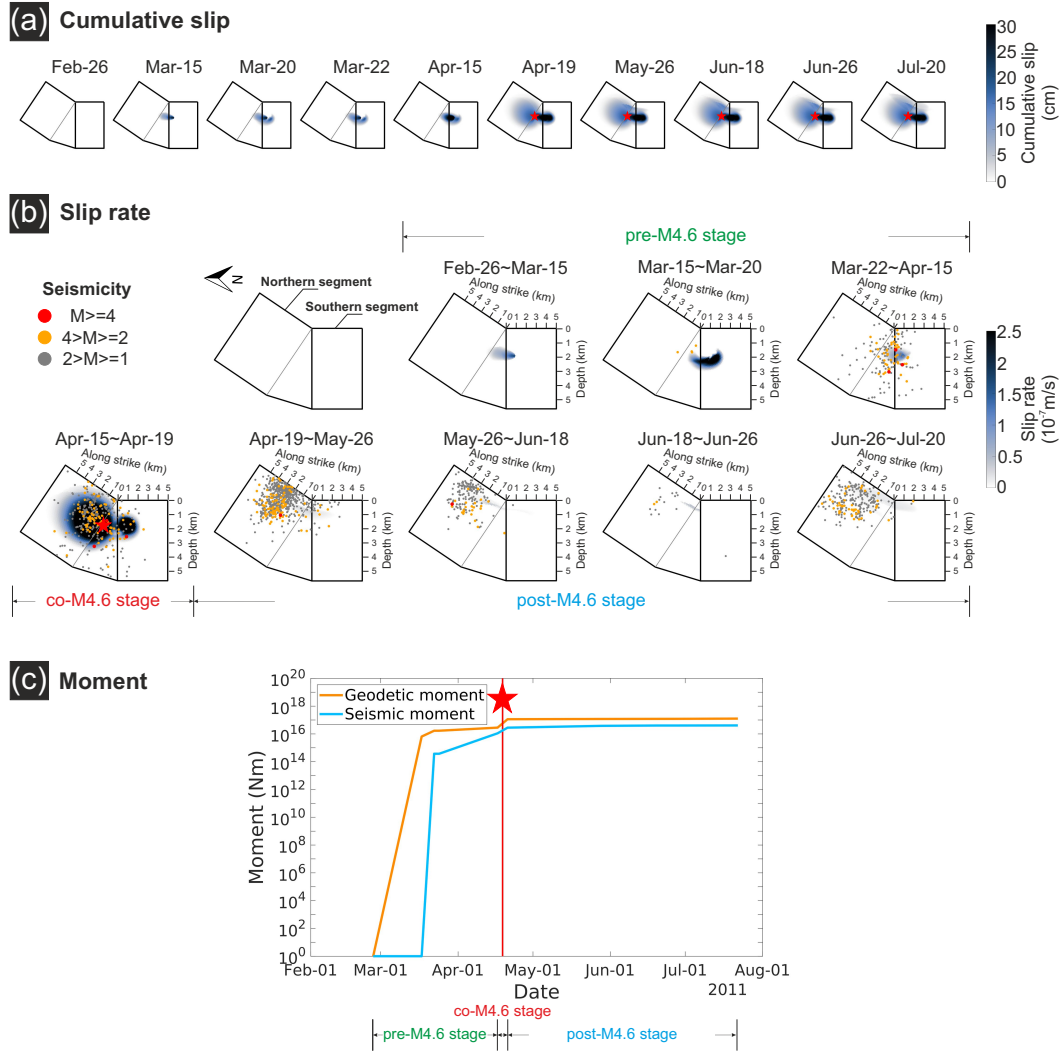


Figure 8. Slip evolution obtained from Time-GICMo inversion of pre-, co- and post-M4.6 stages during 2011 Hawthorne seismic swarm. Image (a) shows the accumulated slip at 10 dates, representing the acquisition time of images in Figures 6a to 6g. Image (b) presents the slip rate during the pre-, co- and post-M4.6 stages. In image (c), blue line shows the cumulative seismic moment based on the USGS earthquake catalog in the region [$38.325^{\circ}\text{N} \sim 38.45^{\circ}\text{N}$, $118.675^{\circ}\text{W} \sim 118.775^{\circ}\text{W}$] (<https://earthquake.usgs.gov/earthquakes/search/>); orange line shows the cumulative geodetic moment, on the basis of estimated cumulative slip in image (a). A variable crustal shear modulus with depth is assumed based on the CRUST 1.0 model in the moment calculation.